GEORG-AUGUST-UNIVERSITÄT
GÖTTINGEN

Bachelor's Thesis

Verbesserung der Elektronen-Emissionsrate in einer offline Mg^+ Elektronenstoß-Ionenquelle für die Laserspektroskopie radioaktiver Ionen

Increasing electron emission rates in an offline electron impact Mg^+ ion source for laser spectroscopy of radioactive ions

prepared by

Lara Maria Bartels

from Osnabrück

at the ISOLDE, CERN and II. Physikalisches Institut, Georg-August-Universität Göttingen

Thesis period:	15th May 2018 until 27th July 2018
First referee:	Dr. Stephan Malbrunot
Second referee:	Prof. Dr. Hans-Christian Hofsäss

Abstract

Conventional collinear laser spectroscopy (CLS) is a powerful tool for the the investigation of nuclear properties of radioactive ion and or atom beams. The work in this thesis contributed to the MIRACLS project, a novel approach to CLS, utilising an electronic ion beam trap, with the potential to greatly enhance the experimental sensitivity.
For demonstration of the feasibility and benchmarking of this new approach in a proof-of-principle experiment, an offline electron impact Mg^+ ion source with the capability of delivering high ion yields over a long lifetime ist required. In this thesis work several modifications in the ion source set-up are explored, aiming at an increase in the number of electrons available for ionisation of Mg atoms whilst allowing for a reduction in heating of the cathode filament. Optimising parameters such as the cathode filament length, shape and position as well as the application of an external electric field are shown to overall increase electron currents by more than a factor of five whilst allowing for the filament heating power to be reduced two 3/4 of its initial value. Additional changes in the treatment of the used thoriated tungsten filaments, so called activation, prior to ion source operation yield electron currents boosted by a factor of more than three at heating powers reduced by a factor of eight. Whilst the rise in electron currents is expected to increase the number of ionisation events and thus Mg^+ ion yields from the source, the reduced heating power of the filament cathode is anticipated to significantly extend the ion source's lifetime.

Contents

1. Introduction **1**

2. Experimental Background **5**

2.1. Collinear laser spectroscopy 5

2.1.1. Observables of collinear laser spectroscopy 5

2.1.2. Collinear laser spectroscopy experiments 7

2.1.3. MIRACLS: A Multi Ion Reflection Apparatus for Collinear Laser Spectroscopy 8

2.2. The MIRACLS ion source 9

2.2.1. Electron impact ion sources 10

2.2.2. A Compact Electron Impact Ion Source for Mg^+ Ions 12

2.2.3. Optimisation for the MIRACLS Proof-of-Principle Experiment 13

3. Thermionic Electron Emission **17**

3.1. Temperature-limited regime 18

3.2. Space-charge-limited regime 21

3.3. Thermionic cathodes for electron impact ion sources 24

3.4. Thoriated tungsten filaments 25

4. Effect of an external electric field on electron rates **31**

4.1. Theoretical expectations 32

4.1.1. Field calculation 33

4.1.2. Space-charge considerations 37

4.2. Experimental set-up 38

4.3. Experimental results 41

4.3.1. Aluminium plate 41

4.3.2. Addition of an outer mesh 43

5. Optimisation of filament parameters **47**

5.1. Calculations based on theory 47

5.2. Experimental procedures 51
5.3. Experimental results 52

6. The Activation Process **59**
6.1. Previous results 59
6.2. Experimental procedure and results 60

7. Conclusion and Outlook **65**

A. Calculation of the Filament Temperature **69**

1. Introduction

The existence of a positively-charged atomic nucleus that concentrates most of an atom's mass in only a small fraction of its volume, was first observed in the now famous Rutherford experiment in 1911. Following this experiment, which has been termed the 'birth' of nuclear physics, further major milestones in the field include the discovery of the proton and the neutron that make up the atomic nucleus and the realisation that atomic nuclei can be unstable and undergo radioactive decay. Despite great achievements in nuclear physics that have been accomplished, a complete understanding of how nuclear properties arise from the underlying fundamental forces is still beyond our reach. While the physics of the electrons of the atomic shell is determined only by electromagnetic interactions, which are fully described in quantum electrodynamics (QED), in the atomic nucleus, the strong force and the weak force are of integral importance in addition to electromagnetic ones. The strong force counteracts the Coulomb repulsion between the positively-charged protons within the nucleus, thus holding the nucleus together and the weak force is responsible for the radioactive decay of nuclei. A number of phenomenological models of the strong, nuclear force have been developed in efforts to describe and predict nuclear properties. Two notable examples of such phenomenological approaches are the shell and the liquid drop model [9].

Investigation of the properties of short-lived exotic nuclei with ratios of protons and neutrons far away from stability contributes to the examination of the nature of the nuclear force. The radioactive ion beam (RIB) facility ISOLDE at CERN produces a wide variety of exotic nuclei, which are used for the study of nuclear physics by different experiments [17].

A powerful tool used for the determination of different ground-state properties of these exotic radionuclides synthesised at ISOLDE is collinear laser spectroscopy (CLS). Ever since the first successful CLS experiments were conducted as early as 1980, continuous improvements and innovations has reserved CLS a central role at the forefront of nuclear physics research [30]. The method takes advantage of the

fact, that the energies of electrons in the atomic shell are affected by properties of the nucleus, giving rise to the hyperfine structure of the atomic spectrum. High resolution measurements of this hyperfine structure performed with CLS give insight into nuclear ground-state properties. In experiments undertaken for example at the COLLAPS beamline at ISOLDE, a radioactive atom or ion beam is collinearly overlain by a laser beam of suitable wavelength. As shown in Figure 1.1, a photon of the appropriate wavelength resonantly excites the atoms or ions within the beam, which subsequently decay into lower-lying states by emission of a fluorescence photon. These fluorescence photons are then detected using photomultiplier tubes (PMT) [30]. By recording the number of photons as a function of laser frequency the hyperfine structure is mapped out. Observation times in current CLS experiments

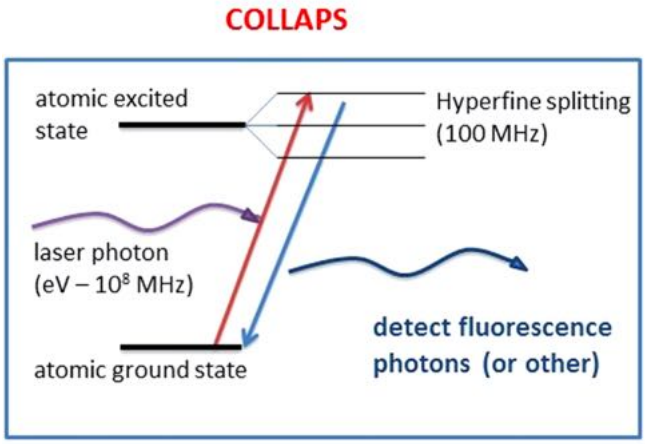

Figure 1.1.: Schematic representation of laser spectroscopy experiments at the COLLAPS beamline at ISOLDE [30].

are limited to a few μs, a limit imposed by the exotic ion's time-of-flight through the laser interaction and optical detection region. The novel MIRACLS approach aims at extending this interaction time, exploiting the full potential of the theoretical upper limit given by the lifetime of the radioactive isotopes. To this end, the bunched radioactive ion beam is trapped in a so called Multi-Reflection Time-Of-Flight (MR-ToF) apparatus [3, 5, 21, 33, 34, 39, 43, 45–47], in which the ions bounce back and forth between a pair of electrostatic mirrors [26]. The laser-ion interaction region, positioned in between the two mirrors, is hence passed many times by the ions. This approach has the potential to enhance the sensitivity of conventional CLS by a factor of 20-600 and allows for CLS measurements to be extended to a number of nuclides which are currently out of reach due to their low production yields [26].

In order to demonstrate the feasibility of this novel experimental approach, a proof-of-principle experiment is currently being set up using stable magnesium isotopes as a first test case. For the tests foreseen with the experimental set-up, an offline Mg^+ electron impact ion source delivering stable beams, preferably at high ion currents, is essential. The goal of this Bachelor thesis is to achieve high, stable and reproducible electron currents in this source facilitating the production of reliable and high-yield beams of magnesium ions.
Chapter 2 of this thesis gives a more detailed introduction to CLS and MIRACLS, followed by the physics of electron bombardment sources as well as the set-up of the MIRACLS ion source. Chapter 3 provides a more detailed account of the physics of thermionic electron emission in the light of its application as a source of electrons in an electron bombardment source. In Chapters 4, 5 and 6 the modification of the ion source currently used at the MIRACLS proof-of-principle experiment that were undertaken as part of this thesis are discussed in detail. The reasoning behind each modification is explained, supporting data from simulations and theoretical calculations is provided and experimental results are presented. Finally Chapter 7 provides a summary of the achievements and discusses other possible modifications for further improving the ion source.

2. Experimental Background

This chapter describes the experimental background of the MIRACLS project with a focus on the MIRACLS ion source used in the proof-of-principle experiment. Section 2.1 provides a short introduction to conventional CLS as a high precision method for the study of basic nuclear properties [30], discussing the nuclear physics of the observables studied as well as experimental aspects. In the final part of the section, the MIRACLS approach to CLS is presented. In Section 2.2 a short introduction to the physics of electron bombardment sources is given before the MIRACLS ion source is discussed in more detail.

2.1. Collinear laser spectroscopy

Laser spectroscopy as introduced before is used to study the hyperfine structure and the isotope shift of ion or atom beams, and opens up access to basic nuclear properties of the rare nuclide under study. CLS is one of two main laser spectroscopy techniques carried out at RIB facilities such as ISOLDE. The defining feature of CLS is the collinearity of the most often continuous laser beam and the beam of atoms or ions to be laser excited. In the second main type of experiment, resonant ionisation spectroscopy (RIS), a resonantly excited atom is ionised by additional lasers [30]. Traditionally, CLS is associated with high resolution and RIS with high efficiency, hence high sensitivity [8]. Today, a significant amount of effort is invested to combine both advantages in CLS and excel with respect to both resolution and efficiency, such as for instance the MIRACLS concept.

2.1.1. Observables of collinear laser spectroscopy

CLS allows to probe a variety of different nuclear properties at RIB facilities in a nuclear model-independent way [8]. These measurements yield access to the nuclear spin, magnetic dipole moment, the spectroscopic electric quadropole moment, and

the mean-square charge radius by studying how interactions with the nucleus affect the electron energy levels and thus the atomic optical spectrum [8]. The most straight-forward way in which properties of the atomic nucleus affect the energies of shell electrons is its positive charge given by the atomic number Z. The atomic number Z corresponds to the number of protons in the nucleus and is of central importance to the Coloumb interaction between the nucleus and the electron shell [14]. The Coulomb interaction is only the strongest of a variety of interactions taking place between an atom's nucleus and its electrons. As early as 1924, spectroscopic data indicated the presence of more subtle interactions [14]. The picture of the nucleus as a point-like positive charge was deemed insufficient for the explanation of these results. Three key ways in which properties of the nucleus affect the electron energy levels have been identified. These are subdivided into the interactions giving rise to the hyperfine structure and the isotope shift. While the isotope shift occurs due to the changes in nuclear mass and volume along isotopic chains, the hyperfine structure is the result of the presence of a nuclear spin [14]. Analogous to the electrons in the atomic shell, the atomic nucleus possesses a nuclear spin I giving rise to a nuclear magnetic moment. If the atomic spin J and the nuclear spin I are both non-zero, their coupling displays as the hyperfine structure [8]. This coupling is mostly dominated by the interaction between the magnetic dipole moment of the nucleus and the magnetic field created by the electrons at the nucleus' position [14]. As the nuclear magnetic moment is outweighed by the electron's magnetic moment by three orders of magnitude, the strength of the interactions with the nucleus' magnetic moment is likewise reduced [14]. The subtle nature of this interaction, which usually corresponds to effects in the order of 1 ppm to 1 ppb when compared to the electronic transitions frequencies, coined the term hyperfine structure, the study of which calls for high resolution spectroscopy [6]. A second contribution to the hyperfine splitting of atomic energy levels is due to the interaction between the spectroscopic nuclear quadropole moment and the inhomogeneities of the electrons' electric field [14]. Following the monopole term in the nucleus multipole expansion corresponding to the Coulomb-interaction mentioned above, the quadropole moment is the second lowest possible contribution [6]. Deviations from a perfect spherical shape of the nucleus give rise to this finite quadropole moment [14].
The isotope shift is the consequence of the change in nucleus' volume and mass between different isotopes of a given element. As the nuclear density remains constant, different neutron numbers within the nucleus introduce changes in the nuclear mean

square radius along chains of isotopes [14, 30]. This change in mass alters the movement of the electrons with respect to the nucleus, introducing an isotope-dependent mass-shift in the optical spectrum [6, 14]. In addition to the mass-shift, the change in volume due to different neutron numbers also affects the electron energies. While based on Gauss's law the potential outside of the nucleus is independent of its shape or size, this does not hold for the inside of the nucleus. As some electron's probability density does not vanish within the atomic nucleus, its volume does affect their energy levels. By comparing the corresponding electronic transition energies of two different isotopes the change in the charge mean square radius can be determined [6].

2.1.2. Collinear laser spectroscopy experiments

In CLS an isotope-separated beam of fast ions or atoms is collinearly overlain with a continuous wave laser beam [6, 30]. When the laser beam frequency matches the atomic transitions of the ions or atoms within the beam, they are resonantly excited into higher energy levels. The number of fluorescence photons emitted perpendicular to the flight direction upon decay to the ground-state, or lower-lying excited states, are detected by a PMT [6, 30]. The hyperfine splitting studied in CLS corresponds to frequency differences of $10 - 1000\,\mathrm{MHz}$. In many ion sources this hyperfine splitting will not be visible due to the Doppler and pressure broadening [8]. The observation of hyperfine splitting is even more demanding for light elements as the hyperfine interactions scale approximately as Z^2 [30]. CLS takes advantage of the reduced longitudinal velocity spread that is achieved through an acceleration of the ion beam resulting in a significant reduction in the Doppler broadening of the spectral lines [6, 30]. Doppler broadening reduced to the same magnitude as the transitions' natural line width can be achieved for acceleration voltages of typically $40\,\mathrm{kV}$ at ISOLDE, also facilitating more efficient excitation for all ions within the beam [30]. In contrast to other laser spectroscopy methods, CLS generally does not rely on laser frequency tuning in order to scan different frequencies, but takes advantage of the Doppler effect instead [8]. While the laser frequency is fixed in the laboratory frame, a secondary acceleration or deceleration voltage is applied to the ion beam prior to the detection region [30]. As the ions' direction of movement is collinear with that of the laser beam, the change in velocity of the ions corresponds to a shift in the ions resonance frequencies by the relativistic Doppler effect [6]. Therefore, scanning through different voltages and thus ion velocities is equivalent to a scanning of the laser frequencies in the laboratory frame [8]. The collinearity

also increases the interaction time between the laser and ion beam in comparison to other geometries, yields a further increase in resolution and has beneficial effects on the tuning stability when compared to scanning of the laser itself [6, 8]. While this results in the excellent resolution of CLS, the method is often inferior in respect to its sensitivity when compared to RIS methods [6]. Over the past decades, multiple novel approaches have contributed to a significant increase in the sensitivity of CLS and the lower limit on the yield for conventional CLS at ISOLDE has reached values as low as 10^3 ions s^{-1} [30]. The most important of those recent developments is the utilisation of ion cooling, accumulation and bunching inside a buffer gas filled linear Paul trap [8, 30]. The sensitivity in CLS is not only limited by the ion yield and the number of photons that can be detected, but also by continuous scattering of laser light, which results in a number of background photons [8]. When operating with a bunched beam, only photons recorded while the ion beam passes through the detection region are regarded to be signal, and photons received at intermediate times between two bunches are considered background [8]. This approach enables background suppression of scattered light by several orders of magnitude [30]. Ion cooling in the Paul trap also decreases the longitudinal energy spread and transverse emittance of the ion beam allowing for a more focussed beam [8]. Due to this decrease in the effective interaction volume, the laser power can be reduced, limiting the photon background and improving the resolution [8].

2.1.3. MIRACLS: A Multi Ion Reflection Apparatus for Collinear Laser Spectroscopy

Large regions of the nuclear chart remain inaccessible by the means of CLS due to limitations in the ion species' production that can be achieved at today's RIB facilities. MIRACLS is determined to overcome these limitations by using the already available ion yield in a more efficient way in order to shed light into these dark stretches of the nuclear chart. MIRACLS' novel approach envisions the use of an electrostatic beam trap, also called MR-ToF device, for the purpose of CLS [30]. The interaction time between laser and ion beam, which is limited to several μs in conventional CLS, amounts to only a minute fraction of the lifetime of radioactive ions available at low energy branches at RIB facilities [26]. It can be extended significantly by trapping the ions such that they pass through the experiment's interaction region multiple times as illustrated in Figure 2.1. Revolution frequencies of

a few kHz are enough in order to increase the sensitivity to the point where one or a few ions suffice to perform CLS, while still taking advantage of the narrowing of the Doppler broadening of the line width by utilising fast beams [30]. This corresponds to an improvement in sensitivity by a factor of 20-600, making the lifetime of the radioactive ion species under study the limiting factor [26]. The prime candidate for investigation using the CLS technique advanced by MIRACLS are ions with closed two-level systems such as Mg^+, in which laser-excited ions decay directly back into the initial state [30]. MIRACLS combines the MR-ToF device with the conventional use of a Paul trap, which utilises a configuration of time-dependent electric fields to trap ions that are subsequently cooled and bunched within the trap [8]. The proof-of-principle experiment is based on a low-energy MR-ToF device operating at a beam energy 1.3 keV, while the MR-ToF for the final MIRACLS experiment has a design energy of 30 keV.

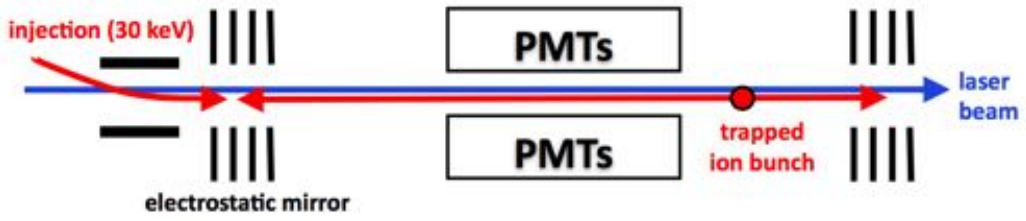

Figure 2.1.: Schematic representation of the principle of utilising an MR-ToF device to increase interaction times in CLS. [26].

2.2. The MIRACLS ion source

In this section the offline Mg^+ ion source in use at the MIRACLS proof-of-principle experiment is described in more detail. First, the mechanism of electron impact ionisation and the working principle of electron impact ion sources are briefly described and the reasoning behind the choice of this source type for the proof-of-principle experiment is presented. The ion source developed by collaboration partners at the GSI Helmholtzzentrum für Schwerionenforschung and the TU Darmstadt is then introduced, which was used as the starting point for the design and construction of the MIRACLS ion source. The final subsection discusses the modifications made to optimise the ion source for its purpose in the MIRACLS proof-of-principle experiment.

2.2.1. Electron impact ion sources

Ion sources can be classified based on a variety of parameters of the source. The most widely used classification of ion sources is based on the ionisation process that is utilised. In electron impact ionisation sources, as indicated by its name, ions are produced via electron impact ionisation. In this ionisation process, an electron strikes a neutral atom, leaving behind a positively-charged ion and an additional, so called secondary, free electron. In order for this reaction to take place, the kinetic energy of the electron has to exceed the first ionisation potential of the atom that is to be ionised [44]. A sketch of the ionisation cross section as a function of the electron energy is shown in Figure 2.2. An initial sharp increase in the cross

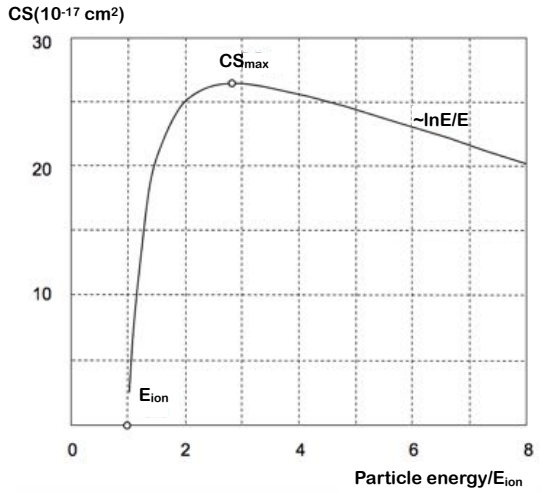

Figure 2.2.: Typical electron impact ionisation cross section (cs) plotted as a function of electron energy in multiples of the ionisation energy E_{ion} [20].

section can be seen when the electron's energy matches the ionisation energy and a maximum is reached for electron energies 3-4 times that value [44]. Electron impact ionisation can be used to create a wide variety of ion species [10]. However, due to the width of the peak, shown in Figure 2.2, notable cross sections of different elements tend to overlap causing contaminants to be ionised in these ion sources in addition to the desired source material [42]. Electron impact ionisation is therefore less selective than other ionisation mechanisms such as resonant laser ionisation or surface ionisation [44].

In an electron impact ion source, primary electrons emitted by a cathode are accelerated by an electric field in vacuum to gain kinetic energies sufficiently high for

ionisation of neutral gas atoms. The exact potential difference between the cathode and anode is chosen such as to optimise the ionisation efficiency discussed above and reduce the contribution from contaminants. The ions created are extracted through either the anode or cathode area, or in a direction perpendicular to the electrons flight path [44]. The main advantage of electron impact ionisation over other sources for singly charged ions is the possibility of very simple and low-cost designs. An additional advantage is the inherently low energy spread of the ions produced by these ion sources. Both advantages come at the cost of rather low ion currents. Different approaches to increase the ion yields have been implemented in electron impact ion sources. One approach utilises magnetic fields in order to effectively trap the electrons in the anode region, thereby increasing the probability of a collision with the gas atoms [44].

A variety of parameters is used to describe the capabilities and properties of ion sources. Amongst them are quality of the produced beam in terms of emittance and brightness, ionisation and material use efficiency, reliability and ease of operation of the source [10]. Surface ionisation sources are severely limited by the relatively high ionisation potential of Mg^+ ions which amounts to 7.65 eV [29], especially if larger intensities are required [44]. The main concern with any type of plasma ion source are the magnetic fields that are crucial for the plasma confinement [44]. Since CLS requires low background fields to avoid Zeeman splitting, the reduction of stray electromagnetic fields that may extend from the ion source to the sensitive components of the set-up is of high importance [29]. As all types of plasma discharge ion sources require magnetic fields of different strengths [44], the utilisation of those sources would have required appropriate shielding and an array of tests to ensure the stray fields do not extend to any sensitive part of the set-up. Moreover, these sources' complexity, costs, and potential beam constraints render their use at MIRACLS unfeasible. This also applies to resonant ionisation laser ion sources, which require a minimum of three high-power lasers of different wavelength to achieve photoionisation of Mg atoms [37].

The top choice for an ion source is therefore an electron impact source abstaining from any additional magnetic fields. Electron-impact sources offer simple, compact and cost-effective construction and maintenance. Although the ion flux produced may be lower than achievable with other sources, it suffices for highly sensitive CLS.

2.2.2. A Compact Electron Impact Ion Source for Mg^+ Ions

The source presented in this section was developed at the GSI and the TU Darmstadt with the goal of building a compact and simple pulsed source of singly charged ions which creates low electromagnetic noise. This is crucial to experimental set-ups including traps such as the Paul trap and the MR-ToF device in the MIRACLS proof-of-principle experiment. A sketch of the set-up of the source can be seen in Figure 2.3. The gaseous magnesium vapour is created in an oven situated on a separate flange and heated directly by a low voltage current. In order to have full control over the oven temperature, which governs the Mg evaporation rate, water-cooling is employed. The stream of neutral magnesium atoms is directed towards the ionisation volume via an opening in its shielding tube facing the ionisation region [29]. The ionisation volume is defined by the anode grid volume. Electrons emitted by a thoriated tungsten filament cathode are accelerated towards the positively biased grid and collide with the neutral gas atoms within the ionisation volume, thus creating Mg^+ ions. The ion extraction from the anode region is controlled by a 1 μs

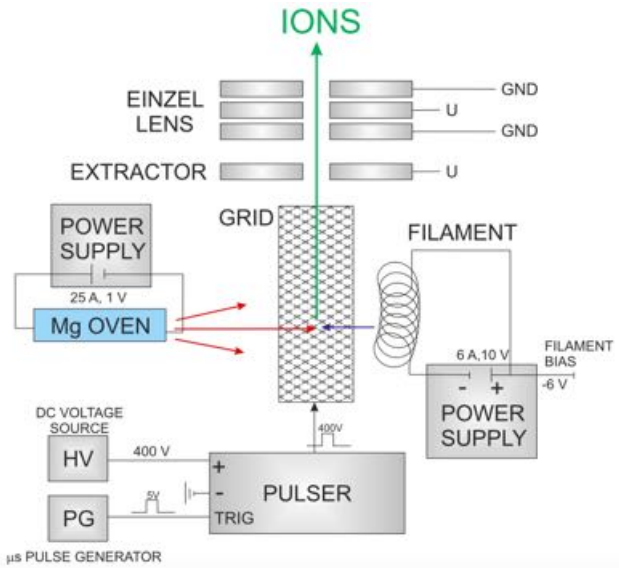

Figure 2.3.: Overview of the electric configuration of the components in the ion source developed by collaboration partners at the GSI and the TU Darmstadt [29].

long high-voltage pulse sent to the grid, raising its potential to 400 V. The change in the potentials causes the ions to be extracted via the extractor and forms a 400 eV, bunched Mg^+ ion beam. It has been demonstrated in [29] that up to 10^6 ions per bunch can be extracted.

2.2.3. Optimisation for the MIRACLS Proof-of-Principle Experiment

The ion source described above was the starting point for the MIRACLS proof-of-principle experiment. A mixture of the stable isotopes 24-, 25- and 26-Mg in their natural abundance was chosen as the source material due to its closed two-state structure, making it suitable for the MIRACLS approach as discussed in section 2.1.3. In order to adapt the ion source to the requirements of the MIRACLS proof-of-principle set-up, changes were made regarding the design and the operation of the source. The most important design change was the inclusion of the oven on the ion source flange as on the right side of Figure 2.4(a). This made the source even more compact and greatly simplified moving the source between different set-ups. However, it comes at the cost of an increased proximity of the oven to the filament due to which the filament contributes to the oven heating in an intricate way. This effect is further boosted by the removal of the water-cooling. This has been shown to result in a fast depletion of the solid Mg supply from the oven over a period of only one week [12]. Improving the electron emission rate of the cathode filament is therefore crucial for reducing the filament heating and its radiative heat load on the oven, such that filament and oven are effectively decoupled thermally. Moreover, a higher electron rate will improve the ionisation efficiency which allows to also lower the Mg emission rate from the oven by reducing its heating via a heating wire. Both effects combined promise to substantially extend the lifetime of the ion source and prevent Mg being deposited on the other components of the ion source.

The initial set-up of the MIRACLS ion source at the start of this Bachelor's project is shown in Figure 2.4(a). The Mg oven on the right side contains a cartridge filled with solid Mg, which is vaporised during operation of the ion source. The oven temperatures can be estimated by use of the indicated thermocouple. The electrons emitted from the filament shown in blue are accelerated towards the grid volume by the potential difference ΔU between the cathode filament and the anode grid. Figure 2.4(b) shows a picture of the resistively heated, glowing filament.

When reaching the grid volume, the electrons have sufficient energy to ionise atoms within the Mg vapour. The Mg ions are extracted from the grid volume by the extractor. The copper beam dump plate seen on the left serves to collect stray Mg atoms. In order to ensure that its temperature is sufficiently low to avoid Mg evaporation, it is connected to the copper rods at the bottom for efficient heat transport

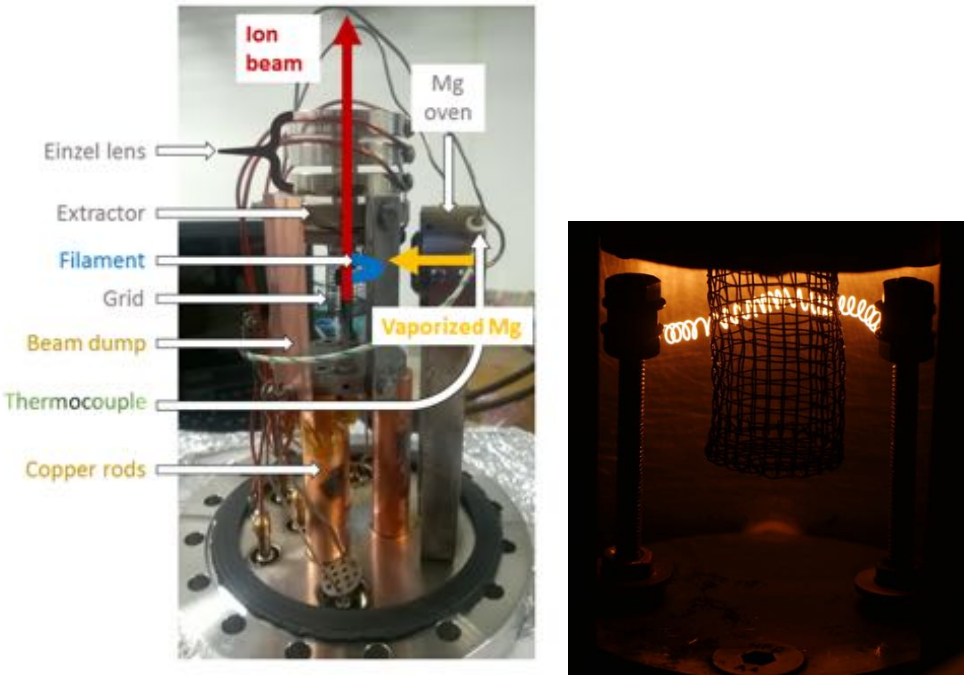

(a) Initial set-up of the MIRACLS ion source [42]. (b) Glowing filament during ion source operation.

Figure 2.4.: An overview of the Initial set-up of the MIRACLS ion source is shown in Figure (a), while a close-up of the glowing filament is seen in (b).

from the radiatively heated beam dump to the outside.

In addition to the changes in design, a major change has also been made to the mode of operation by abandoning the pulsed mode and switching to a direct current mode. As the MIRACLS set-up includes a buffer-gas filled Paul trap for cooling and bunching of the ion beam, no inherently pulsed operation of the ion source is required. This is expected to result in an increase in the overall ion yield from the source, which is otherwise limited by the pulser frequency. In the case of the MIRACLS ion source the ions are extracted in a continuous mode by a constant potential difference between the extractor and the grid. To facilitate the formation of a continuous beam, the grid is biased to 250 V with respect to the MIRACLS beamline ground. In the current set-up the ionisation efficiency of the magnesium gas reaches its highest value for potential differences of about $20 - 30$ V between the cathode filament and grid anode. This value is predominantly determined by the ionisation cross section of the magnesium atoms, which is expected to peak at electron energies corresponding to three times the Mg ionisation potential of 7.65 eV and amounts to approximately 23 eV [20]. As the electrons emitted by the filament

posses little kinetic energy, the electrons' kinetic energies correspond to the potential difference between the emission point on the cathode and the anode. Due to the presence of space charges, higher potential differences result in higher electron currents at the anode grid, as will be discussed in Chapter 4. Therefore the optimal value for the potential difference is slightly higher in this case.
As a constant bias voltage needs to be applied to the grid, the continuous mode of operation requires floating of the filament heating power supply to maintain the acceleration voltage of $\sim 30\,\mathrm{V}$. It has been shown experimentally that the current at the grid decreases significantly when floating the filament heating power supply, ultimately resulting in a decrease of the ion current produced. The increasingly positive bias voltage of the filament with respect to the surrounding grounded parts of the set-up exhibits this detrimental effect due to its tendency to enhance present space-charge effects. An additional decrease in electron emission is due to what amounts to a 'reverse' Schottky effect as the resulting electric field increases the potential barrier which the electrons need to overcome at the filament surface instead of lowering them. To overcome these limitations, several modifications were made to the ion source set-up described in this section in order to increase the electron emission rate and therefore the ion yield. The reasoning behind these modifications as well as the results of experimental test are discussed in Chapters 4 and 5, while findings regarding changes in the filament conditioning are presented in Chapter 6.

3. Thermionic Electron Emission

Thermionic emission is just one of a variety of different mechanisms by which electrons are emitted from a solid cathode. These mechanisms are characterised by how the electrons overcome the finite potential barrier at the cathode's surface. In most metals this potential barrier, which is referred to as the work function of a material, amounts to $1\,\mathrm{eV} - 5\,\mathrm{eV}$ above the Fermi energy [19, 20]. The different types of electron emission are sketched in Figure 3.1. Electrons from within the

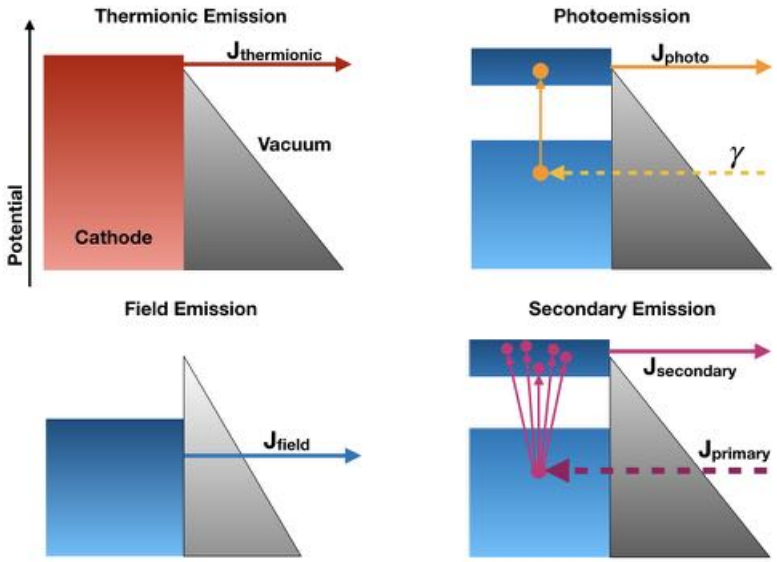

Figure 3.1.: Illustration of the different mechanisms of electron emission. The grey triangles correspond to the potential barrier between the cathode material on the left and the vacuum on the right. The coloured rectangles represent the electrons within the cathode. Created based on [19].

metal are emitted after either gaining enough energy to overcome the barrier or by tunnelling through it. For tunnelling to occur with a probability that results in a detectable number of emitted electrons the barrier needs to be sufficiently thin. In field emission, electric fields of immense strength are applied between the cathode

and an anode enabling an appreciable number of electrons to tunnel through the barrier and leave the solid. All other emission mechanisms rely on the transfer of sufficient energy to the electrons within the metal to facilitate emission over the barrier. In photoemission this energy is transferred to the electrons from absorbed photons, in secondary emission they gain energy in collisions with high-energy incident primary electrons. The final mechanism of electron emission, which is to be discussed in more detail in this chapter, is thermionic emission. In this emission mechanism the increase in the kinetic energy of the electrons is brought about by heating the cathode to high temperatures. Temperatures need to be sufficient such that electrons in the high-energy tail of the Maxwell-Boltzmann distribution have kinetic energies high enough to overcome the barrier at the surface.
The first section of this chapter will discuss the temperature-dependence of thermionic emission in greater detail. The emission rate can be studied experimentally by measuring the current density J received at an anode. However, the number of electrons emitted by means of any of the mechanisms described above does not necessarily match the current received at the anode. When large numbers of electrons are being emitted from the cathode, the space charges in the region between the anode and cathode can become the limiting factor of the current flowing to the anode [19]. The second section will discuss these space-charge limitations whilst focusing on the case of thermionic emission and the transition from one regime to the other will be explored. Thermionic cathodes are then briefly introduced in general before the final section of this chapter discusses thermionic properties of thoriated tungsten and its advantages over pure tungsten as a cathode material.

3.1. Temperature-limited regime

Thermionic emission in vacuum has been the object of a great deal of research and controversy in the early 19^{th} century. The development of thermionic cathodes was an important contribution to the beginning of the electronics industry [36]. In 1901, Richardson derived an equation describing the (surface) current density in thermionic emission based on the theory of electrons in metals advanced by Drude and Thomson. Richardson argued that the 'free' metal electrons relevant for thermionic emission follow a velocity distribution given by Maxwell-Boltzmann, and at high temperatures a small fraction of electrons in the high energy tail have sufficient energy to overcome the potential barrier at the surface [36]. His discoveries

surrounding the field of thermionic emission were honoured with the Nobel prize in physics in 1928 [36]. According to Richardson, the saturation current density J_R at a temperature T is given by the equation

$$J_R = A_R T^2 \exp\left(-\frac{\Phi}{k_B T}\right), \tag{3.1}$$

where A_R is the material-dependent Richardson coefficient, Φ is the work function of the material and k_B is the Boltzmann constant [19]. A lower value of Φ is desirable in a thermionic emitter as higher emission rates can be achieved at a given temperature [20]. The Richardson coefficient A_R for any material can be obtained from the theoretical value A_{free} for free electrons

$$A_{free} = 4\pi \frac{m_e \epsilon_0 k_B^2}{h^3} = 120\,\mathrm{A/cm^2K^2}, \tag{3.2}$$

where h is Planck's constant and ϵ_0 the vacuum permittivity, by replacing the free electron mass m_e by the effective electron mass m_e^{eff} in the solid. Thus the interaction between electrons and holes is taken into account [20]. In the temperature-limited regime the work function as well as the Richardson coefficient of any material can be obtained from the slope of so called Richardson-plots in which $\ln\left(\frac{J}{T^2}\right)$ is plotted as a function of $\frac{1}{T}$ as shown in Figure 3.2 [28].

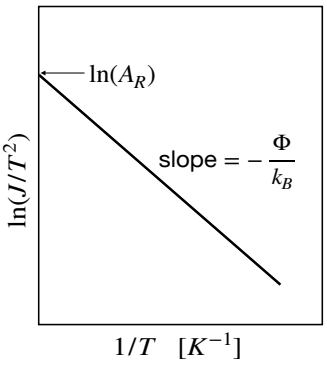

Figure 3.2.: Example of a Richardson plot. The current density J and the temperature T are plotted as J/T^2 over $1/T$. Figure created based on [28].

As early as 1914, Schottky realised that the main contribution to the potential barrier at the surface is due to the image charge at the surface of a conductor as indicated in Figure 3.3 [36]. Therefore if a cathode is negatively biased with respect

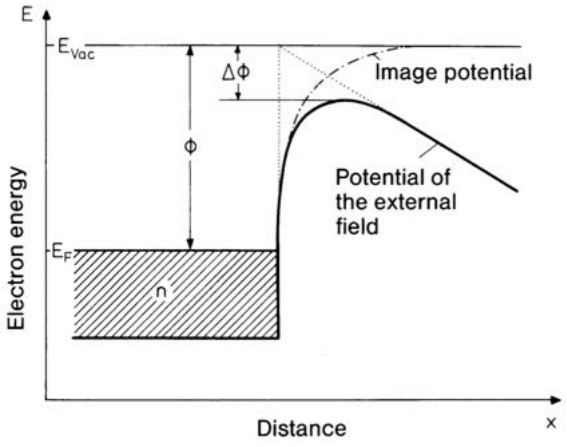

Figure 3.3.: Schematic representation of thermionic emission from a metal. The dashed line corresponds to the absence of external fields, the solid line illustrates the lowering of the potential barrier due to an external electric field, the so called Schottky effect [16].

to its surroundings the thermionic emission is enhanced, as the resulting electric field lowers the potential barrier the electrons have to overcome at the surface to 'escape' from the filament. This so called Schottky effect is reflected in a modified version of Equation 3.1 by an effective lowering of the work function due to the presence of an electric field of strength F at the cathode surface. The modified work function Φ is given by [16]

$$\Phi = \Phi_0 - \sqrt{\frac{e^3 F}{4\pi\epsilon_0}}, \tag{3.3}$$

where Φ_0 is the work function at zero applied field and e is the elementary charge. Due to their cathode-anode configuration, the Schottky effect is present in all ion sources. For realistic set-up configurations in an ion source the increase in electron emission rates has been shown not to exceed 5% [20]. However, the saturation current density described by Equation 3.1 may not be reached in cases where the potential difference between anode and cathode is small and space-charge effects at the cathode discussed in the next section come into play.

3.2. Space-charge-limited regime

At very high temperatures copious numbers of electrons given by Equation 3.1 are emitted from a thermionic cathode. However, when increasing the cathode temperature beyond a certain point, the electric field determined by the applied potential difference between cathode and anode is not sufficient to draw away all of the electrons from the cathode region. This results in the formation of an electron cloud crowding the space surrounding the cathode. The effects of this electron cloud are referred to as space-charge effects. The negatively charged cloud screens the electric field from the surface of the cathode and limits the number of electrons being accelerated to the anode due to the electrons' mutual repulsion [19]. The effect of this electron cloud on the electron's potential energy is illustrated in Figure 3.4. A potential energy maximum emerges between the cathode and the anode at a distance x_m from the cathode resulting in a retarding potential to the left of this point. A significant fraction of the electrons emitted from the filament are reflected

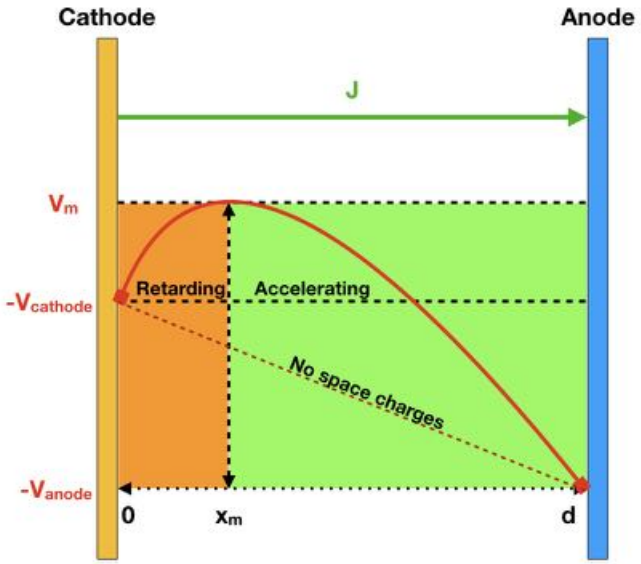

Figure 3.4.: Potential energy of an electron between two parallel plates as a function of distance from the cathode. The two cases including (solid red line) and excluding (dashed red line) the presence of space charges can be compared. Created based on [19].

off this potential barrier and move back towards the filament [24]. Only electrons with sufficient energy to overcome this additional barrier contribute to the current flow to the anode [24].

It is important to note that even in the space-charge-limited regime, the number of electrons emitted is still given by the Richardson Equation 3.1. The current that can be extracted from the electron cloud surrounding the cathode and is received by the anode, however, is not given by the Richardson equation and depends more strongly on the electric fields acting upon the electrons within the cloud. More intense accelerating electric fields between cathode and anode translate into more kinetic energy being transferred to the electrons within this field and hence an increase in current as more electrons have the ability to overcome the potential barrier. For the same reason space-charge effects are intricately linked to the geometry of the set-up [19] whilst in the temperature-limited regime only the surface area A of the cathode is relevant for the emitted current I via $I = J \cdot A$. For a parallel plate configuration of cathode and anode the current density J_{CL} that is received by the anode in the fully space-charge-limited regime is given by the Schottky-Langmuir or Child-Langmuir law

$$J_{CL} = K\Delta U^{3/2}\frac{1}{d^2}, \tag{3.4}$$

where ΔU is the potential difference between cathode and anode, d the distance between the two and $K = \frac{4}{9}\epsilon_0\sqrt{\frac{2e}{m_e}}$ is a constant where m_e corresponds to the electron mass [41]. It has been shown that

$$J_{CL} \propto \Delta U^{3/2} \tag{3.5}$$

is not limited to the case of parallel plates but holds for any cathode anode geometry [4]. E.g. [20] employs the distance dependence given by Equation 3.4 in a configuration consisting of a cathode wire and an anode similar to the MIRACLS ion source. Deviation from Child's law are expected for small accelerating voltages where the electrons' initial kinetic energies are no longer negligible [22]. In the space-charge-limited regime the current becomes independent of the cathode material [24]. However, the cathode material does affect the temperatures and applied potentials at which the transition from the temperature-limited to the space-charge-limited regime takes place. Such a transition is shown in Figure 3.5 in which the current received at an anode is plotted as a function of filament temperature. When the number of electrons received by the anode is equal to that emitted from the cathode the current is deemed saturated and temperature-limited [24]. This corresponds to the left hand side of Figure 3.5, where the current density increases according to the Richardson Equation 3.1. In the transition region space-charge effects as

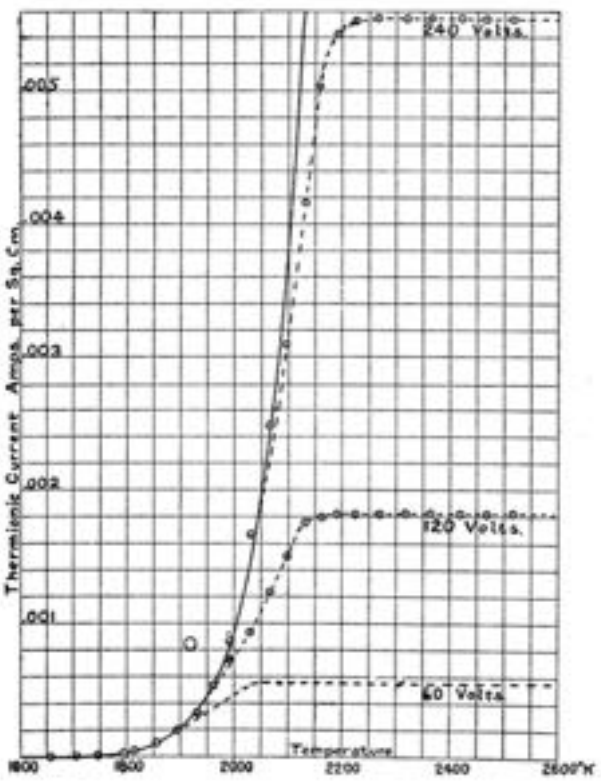

Figure 3.5.: Thermionic current density as a function of filament temperature. A transition from temperature-limited to the space-charge-limited regime for different potential differences between cathode and anode can be observed. See text for details [22].

well as temperature limitations become relevant and parameters from both Equations 3.1 and 3.4 determine the current flowing to the anode. Finally, on the right hand side of Figure 3.5, the current does no longer increase with increasing temperature and the current becomes fully space-charge-limited. Two important conclusions can be drawn from Figure 3.5. Firstly, the current saturates at lower temperatures for lower potential differences between anode and cathode. Secondly, the saturation current that can be reached in the space-charge-limited right part of the plot is independent of the filament temperature, but depends on the potential difference. Therefore heating the cathode at temperatures that exceed those required to reach space-charge currents for a given set-up is highly inefficient [19]. For a stable source of electrons, operation close to the transition region is desirable, where full advantage is taken of the maximally available electron current in the space-charge-limited regime [19]. This minimises the inefficient heating and cathode life-time limitations

due to high temperatures while still taking advantage of space-charge effects [19]. In fact, space-charge effects are not always undesirable for cathode operation. Their presence results in a smoothing of the emitted beam in space and makes the emitted current less sensitive to small changes in the emission rates [19]. The presence of positive ions in the space-charge cloud can partially balance the repulsive effect of the electron cloud and lead to an increase in the space-charge-limited current. It needs to be pointed out however, that this neutralisation might come at the prize of increased residual gas pressures which can in turn reduce the currents received [36]. In general the presence of positive ions is ascribed a positive effect on thermionic as well as field currents [19]. The sputtering away of surface contaminants might be one of the contributing factors of this effect [2].

3.3. Thermionic cathodes for electron impact ion sources

The thermionic cathode is a component of crucial importance in electron impact ion sources, often being the limiting factor in the source's lifetime and overall performance. A perfect cathode would optimise the electron emission rates by combining a low work function and high melting point, allowing for efficient heating, with chemical inertness and the ability to withstand ion bombardment. It should neither be affected by depositions of the source material or exposure to air nor should the evaporation rates be too high. Finally it should be easy to manufacture and handle. Typical cathode materials include tungsten, tantalum and since recently LaB_6, each with their own advantages and drawbacks regarding reactivity, operating temperatures and handling [48]. In the most simple case of a directly heated cathode, a filament is resistively heated by passing a heating current through it [44]. In indirectly heated cathodes the energy required for the increase in temperature is supplied by a current of impinging electrons, ions or radiation [48]. Only resistively heated filament cathodes are considered in all subsequent discussions.
Despite its high work function of 4.56 eV, tungsten is used as a thermionic cathode material in a wide variety of applications. This is mostly due to the metal's mechanical strength and high melting point which enables operation at high temperatures and electric fields resulting in adequate emission levels for the use in electron impact ion sources, albeit at low efficiency [15]. Despite its high melting point, tungsten cathodes should be operated at the lowest possible temperatures in order to prevent

a shortening of its lifetime due to increased evaporation at high temperature [20]. The thermionic properties of tungsten filaments can be significantly improved by the addition of thorium or alkali and alkaline earth layers to a tungsten filament [19]. The use of thoriated tungsten filaments as thermionic cathodes is discussed in the next section.

3.4. Thoriated tungsten filaments

Thoriated tungsten filaments usually contain 1-2% weight of thoria ThO_2 [25]. Thoriated tungsten is superior to tungsten in its efficiency as a thermionic emitter, allowing for the heating power required to achieve a given emission rate to be reduced by a factor of six [15]. Figure 3.6 compares the saturation current density that can be obtained from tungsten and thoriated tungsten filaments according to Equation 3.1 as a function of temperature. It can be seen that the increase in emission capabilities at a given temperature spans multiple orders of magnitude and the same current densities are reached at much lower temperatures for thoriated tungsten. In order to take advantage of this, special treatment of the thoriated filaments prior to their operation is required, as thorium only enhances emission if it is present at the filament's surface in metallic form [25].

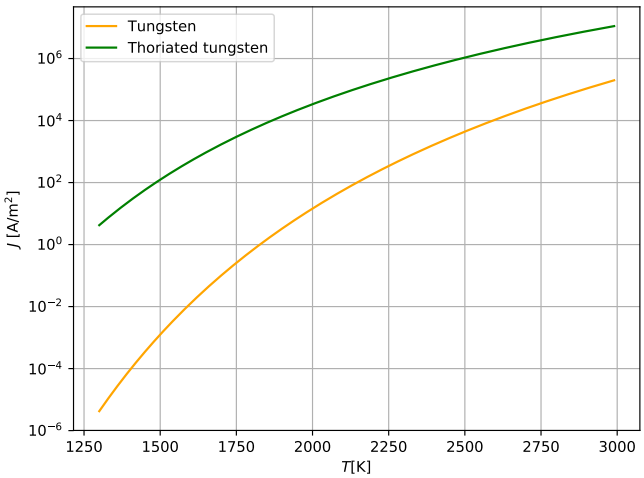

Figure 3.6.: Saturation current density $J[\mathrm{A/m^2}]$ as a function of temperature for tungsten and thoriated tungsten.

If operated at the customary operating temperatures for tungsten filaments of $2250 - 2500\,\mathrm{K}$ [13], no difference in emission rates from thoriated tungsten and pure tungsten filaments can be observed [25]. In 1913 Langmuir demonstrated that a special heat treatment is necessary in order to obtain electron emission rates of up to five orders of magnitude higher than that of pure tungsten [35]. This increase in emission is a result of a decrease in the work function from 5.4 eV to 2.6 eV [27]. The exact change in work function is determined by the surface coverage of thorium atoms on the tungsten surface. Surface coverage $f = \frac{\sigma}{\sigma_0}$ is defined as the ratio between the number density of adsorbed thorium atoms σ at some given temperature and σ_0 for which the work function is minimised. The work function is minimal for a monolayer of thorium atoms [13] corresponding to a surface coverage of $\sigma_0 = 4.2 \cdot 10^{14}\,\mathrm{atoms/cm^2}$ [35]. The work function Φ as well as the Richardson coefficient A_R are plotted as a function of surface coverage f in Figure 3.7. From Figure 3.7 it can be deduced that there is an optimal value of the surface coverage minimising the work function and thereby maximising the emission capabilities of the filament. If the thorium coverage is increased any further, the work function increases again and approaches that of pure thorium of 3.4 eV [19, 35]. The minimum

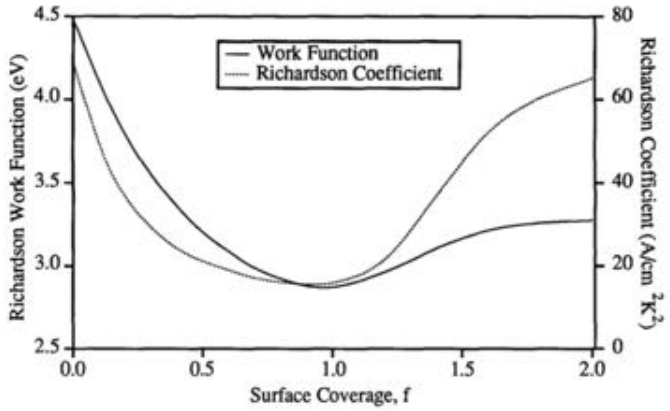

Figure 3.7.: Work function Φ and Richardson coefficient A_R of thoriated tungsten as a function of the surface coverage f [35].

seen in Figure 3.7 is explained by the dipole nature of the bond formed between tungsten and thorium which induces changes in the potential close to the surface ultimately resulting in the observed change in the material's work function [35].
The most recent account of the activation procedure for maximising the emission capabilities of thoriated tungsten filaments is found in [35].

The process can be divided into two main steps. First, in the flashing process, the filament is heated to high temperatures in order to reduce the thorium oxide inside the filament to metallic thorium, which diffuses to the surface of the filament in the second, so called activation step of the process. In the first step the filament is flashed at high temperatures $> 2600\,\mathrm{K}$ to reduce the thorium oxide ThO_2 and produce metallic thorium [35]. Flashing times between 30 s and 3 minutes are recommended [25]. Afterwards, most of the thorium is present in the wire in the form of small granules about a micron in diameter [7]. At such high temperatures the entire supply of thorium on the surface evaporates and activation of the filament at lower temperatures is required to replenish this supply [1]. For activation the filament is operated at $2000 - 2300\,\mathrm{K}$ for 15-30 minutes [15, 35]. At these temperatures the diffusion rate of thorium from the interior to the filament's surface is high compared to the evaporation rate of thorium from the surface [35]. Thorium accumulates at the filament surface in a layer not more than one atom thick and results in changes to the work function as seen in Figure 3.7 [36]. The increase in electron emission rates over time in the activation process is shown in Figure 3.8. The measurements presented in Figure 3.8 were taken at a fixed testing temperature

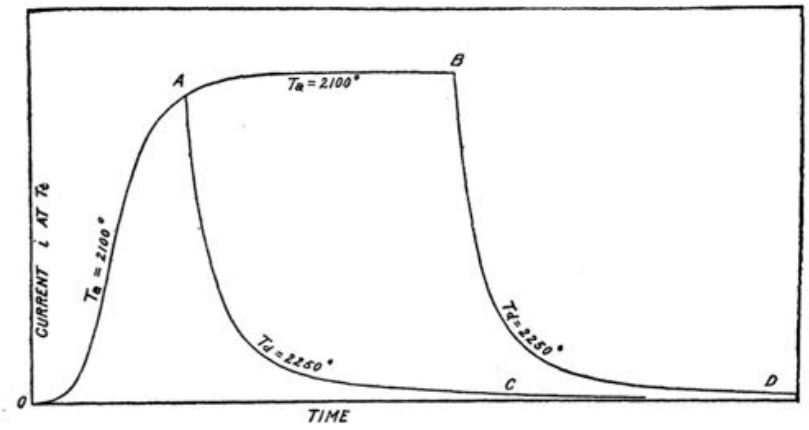

Figure 3.8.: Emission currents over time showing activation at 2100 K and deactivation processes at 2250 K [25].

T_t significantly below activation and deactivation temperatures. Deactivation of the filament, explained later in this section, is also shown.

Once the filament is activated, the filament temperature needs to be reduced in order to achieve stable operation whilst maintaining the low work function. Operating temperatures between 1400 and 1800 K are recommended at which both evaporation and diffusion rates are small [7, 35]. Even over prolonged periods of time of up

to 1000 h the thorium diffusion rates from the interior are high enough to compensate for the thorium desorption from the surface [7]. Following the activation process, the filament temperatures should at no point exceed 2200 K, otherwise deactivation of the filament, as seen in Figure 3.8, occurs and the thermionic properties of the filament drop back to those of pure tungsten [25, 35]. In the deactivation temperature regime evaporation from the surface exceeds the diffusion of fresh thorium from the interior. If the filament is operated at such high temperatures for extended periods of time, the thorium supply within the wire is gradually depleted [7]. While activation of the filament at lower temperatures lowers the rate of activation, studies in [7] show that it results in an increase in the maximum value of thorium coverage f. It was also demonstrated, that an oxygen depletion is associated with the increase in thorium coverage. Even temperatures as low as 2000 K are shown to result in a significant decrease of the thorium surface coverage after some time, while for 1800 and 1450 K "quasi-static" states are reached.

The surface layer of metallic thorium is very sensitive to oxidisation and thus to contamination by gases. Therefore the filament's thorium layer must be protected during operation either by high vacuum or by the presence of substances that readily oxidise, such as sodium, magnesium or calcium [25]. In general, residual gas results in a decrease in the thermionic currents that can be obtained [22]. The effects of poisoning by oxygen and other electronegative elements are especially detrimental regarding the emission capabilities of both thoriated and pure tungsten cathodes. Oxidation of the thorium brought to the surface effectively reverses the effect of flashing and the work function increases. At high oxygen pressures and temperatures the oxidation of tungsten can more than double the work function of pure tungsten [15]. For this reason degassing the filament by operation at higher than nominal temperatures and subsequent flashing of the filament at high temperatures around $3000K$ are also beneficial for pure tungsten cathodes due to a cleaning effect [15].

In addition to the effects of oxygen, the presence of carbon has a manifold and important impact on the emission capabilities of thoriated tungsten filaments. Emission rates drop significantly in the presence of elemental carbon or tungsten carbide if temperatures exceed 2200 K. In contrast, at temperatures below 2200 K so called carburisation is beneficial for filament operation. It minimises evaporation rates and thus improves the lifetime of the filament as well as boosting electron emission rates [27, 38].

Additional methods for achieving activation of the filament whilst omitting the high temperature treatment are described in the literature. The first method is reported in [1], where activation of a thoriated tungsten filament caused by breakdowns at high fields of $10^6\,\mathrm{V/cm}$ is observed, which is most likely caused by positive ion bombardment of the cathode [1]. High energy positive ion sputtering as well as electron bombardment of cathodes is also used as a way of achieving activation in [27] and [7, 11]. One has to be careful when it comes to the nature of these ions however, as deactivation of thoriated tungsten cathodes occurs when impinging positive oxygen or carbon ions form compounds with the tungsten which cover the filament surface [22]. Argon ions on the other hand have been shown to sputter away in these compounds and are used for activation [11, 22].

4. Effect of an external electric field on electron rates

As motivated in Section 2.2, the direct current mode of the MIRACLS ion source requires a positive bias voltage of the filament heating power supply and the anode grid of 220 V and 250 V, respectively. This positive bias voltage has detrimental effects on the electron current received at the anode grid which can be seen in Figure 4.1. The electron current measured at the grid rapidly decays with the increasing bias voltage, resulting in a substantial decrease in the number of electron available for ionisation during the operation fo the ion source. To overcome

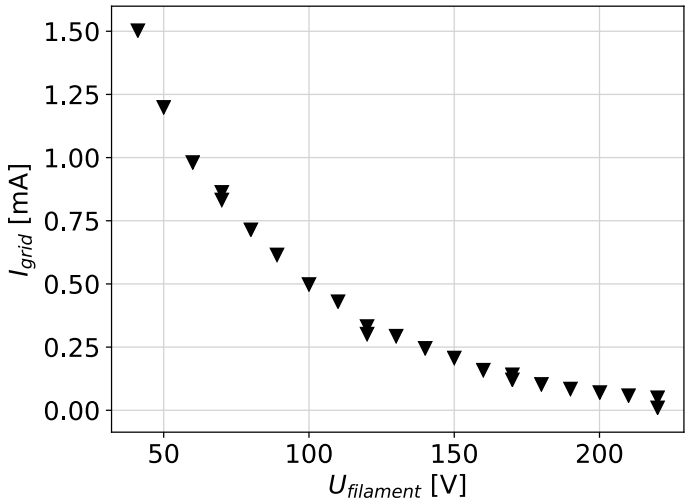

Figure 4.1.: Electron current I_{grid} received at the anode grid as a function of the bias voltage $U_{filament}$ applied to the filament. The accelerating potential difference $\Delta U = 30\,\mathrm{V}$ between anode grid and filament is constant.

this limitation imposed by the floating of the filament heating power supply in the MIRACLS ion source, an outer biasable mesh is included in the set-up which is foreseen to reduce the positive relative bias voltage of the filament. Compared to the results shown in Figure 4.1, this is expected to make the electron currents

largely independent of the filament bias voltage and hence to significantly increase the ion yield of the source. The position of the mesh within the set-up is sketched in Figure 4.2.

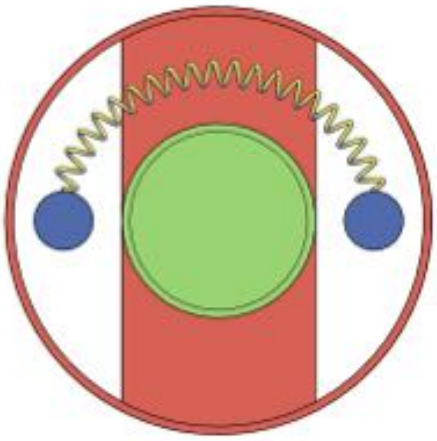

Figure 4.2.: Top view sketch of MIRACLS' ion source set-up. In addition to the two leads (blue), the helical filament (yellow) and the anode grid (green), the new outer mesh (red) is included.

4.1. Theoretical expectations

The idea behind integrating an additional outer mesh in the set-up is the reduction of the positive bias voltage of the filament with respect to its surroundings. A negative bias voltage of the cathode lowers the potential barrier the electrons have to overcome in order to leave the filament via the Schottky effect, as described in Section 3.3. More importantly, the outer mesh brings about changes in the electric field that are expected to diffuse the space-charge cloud surrounding the filament. This should lead to an increase in the number of electrons emitted from the filament via thermionic emission and which is received at the anode, a higher number of ionisation events and eventually Mg^+ ions forming the ion beam. An increase in the outer mesh potential is beneficial for the ion source performance, as long as the outer mesh potential is not significantly higher than the anode grid potential i.e. provided that not too many of the electrons are accelerated towards this additional mesh instead of to the anode grid.
In the first part of this section, the effect of the external mesh on the electric fields

in the set-up is studied neglecting space-charges. Based on these calculations, an expectation for the effect of the outer mesh in the presence of space-charges is then developed and later compared to experimental results.

4.1.1. Field calculation

In order to study the effect of an additional outer mesh on the electric fields at and around the filament in the ion source, the anode grid, the filament and the outer mesh were implemented with a cylindrical symmetry in SimIon [40]. The employed distances approximately match those of the real set-up since the installation of the filament can only be controlled to a certain level of precision. No major deviations are expected from possible discrepancies as only the relative values and their orders of magnitudes are of interest for the following qualitative discussions.
The electric potentials as well as the electric fields were calculated for the nominal potentials of 250 V at the anode grid and 220 V at the filament. The simulations were carried out for potentials of $U_{mesh} = 0\,\mathrm{V}$, resembling the situation prior to the modifications of the ion source in this work, as well as $U_{mesh} = U_{filament} = 220\,\mathrm{V}$ applied to the outer mesh. The latter value of U_{mesh} was chosen to maximise electron currents whilst avoiding the onset of current to the outer mesh. These two cases are compared in Figure 4.3 in which the calculated potential energy and radial electric field are plotted as a function of the radial position. Taking advantage of the cylindrical symmetry, the radial electric field is defined as the projection of the electric field onto the radial direction in cylindrical coordinates at any given point. The force F acting on an electron in an electric field E is given by $F = -e \cdot E$. Due to the electrons negative charge, positive electric fields thus correspond to an electron acceleration towards the centre of the grid and vice versa. In the case of the grounded outer mesh shown in blue, the electrons face a steep and high potential energy well on the filament side facing the outer mesh. The effect of the mesh grounding even extends to the other side of the filament facing the grid. When moving from the filament towards the anode grid, the electrons' potential energy first increases, passing a shallow and rather broad maximum, before the potential drops steeply to the fixed value of the anode grid. Electrons emitted from the filament thus find themselves in a potential well with a high wall to the right and a small maximum towards the anode grid. This is also reflected in the corresponding plot of electric field in the lower plot of Figure 4.3. The electric fields on both sides of the filament correspond to a force pushing the electrons back towards the filament.

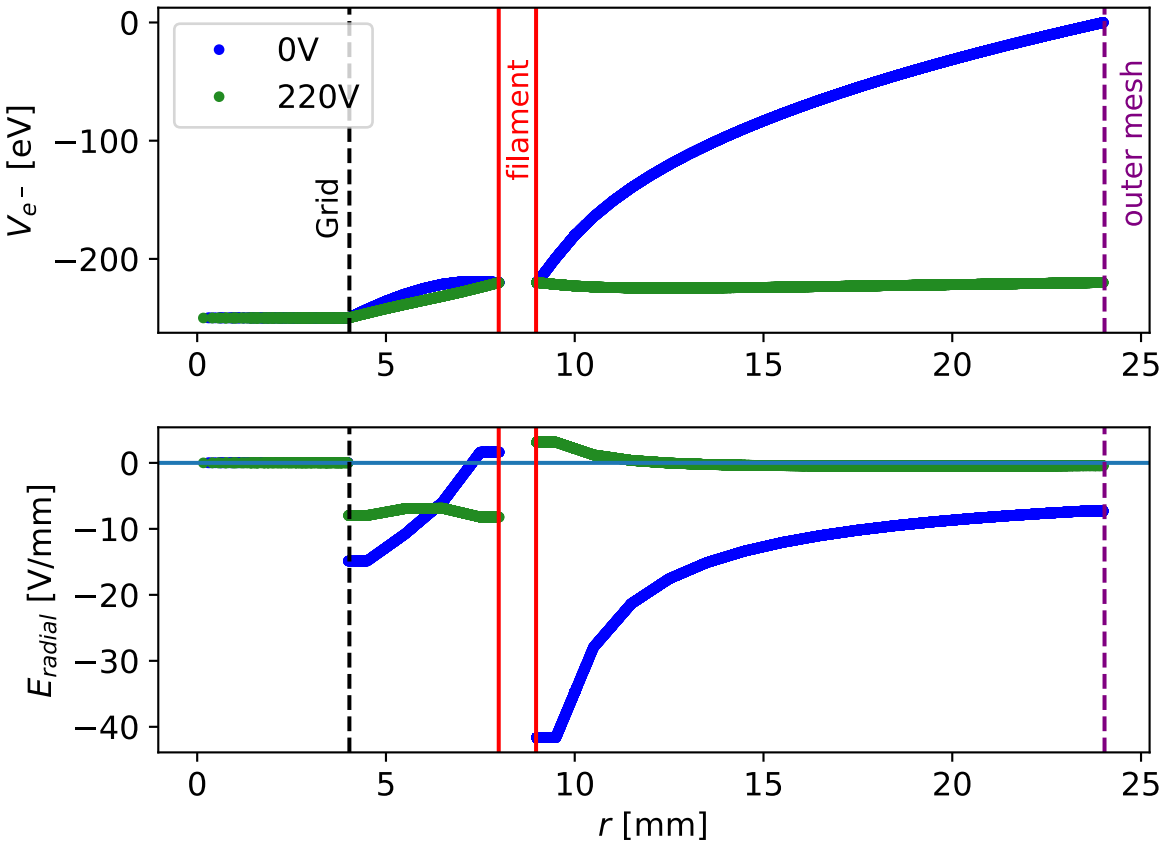

Figure 4.3.: Electron potential energy V_{e^-} and radial electric field strength E_{rad} as a function of position between grid, filament and outer mesh obtained from SimIon calculations. Voltages of 0 V or 220 V are applied to the outer mesh. Filament and grid are held at 220 V and 250 V, respectively, as typically used in the MIRACLS ion source. The vertical lines only indicate the positions of the different components along the axis and are not meant to indicate their extent along any additional axis.

Towards the grid, the electrons only feel a weak electric field pushing them back, corresponding to the small potential barrier in Figure 4.3. Electrons that overcome the potential barrier are accelerated towards the anode grid.

The potential for the case in which the outer mesh is on the same potential as the filament is plotted in green in Figure 4.3. The potential energy distribution is very different from that one for the grounded mesh. The filament constitutes a maximum of the potential energy rather than a minimum. On the side facing the outer mesh, the potential passes through a very shallow minimum before increasing back up to the value at the filament. The potential distribution in the region between

the filament and the cathode grid is linear to a good approximation and thus resembles the potential expected between two parallel plates. The contrast between the 0 and 220 V applied to the mesh is most striking in the distribution of the radial electric field strength. While for a grounded mesh the electric fields at the filament tend to trap emitted electrons near the filament, the electric fields in the case of 220 V accelerate the electrons away from the filament on both sides of the filament. In the case of the grounded mesh, the electric fields tend to increase the potential barrier due to a reverse Schottky effect, while in the case of $U_{mesh} = 220\,\mathrm{V}$ the potential barrier is lowered. The electric fields on the outer mesh side of the filament decrease as electrons move away from the filament towards the mesh. When the electrons are in close proximity to the mesh, the electric field even changes sign and tends to repel the electrons away from the outer mesh. [1] As the electron are emitted in all directions from the filament, only a very small fraction will have initial momenta only in the plane spanned by the filament. Most electrons reflected by the mesh will therefore pass below or above the filament and reach the anode grid instead of being recollected by the filament. Hence, the electric fields in the case of $U_{mesh} = U_{filament}$ facilitates the extraction of electrons away from the filament in both directions when compared with the grounded mesh whilst avoiding the collection of electrons at the outer mesh.

Focusing effect

The field calculations also indicate that the additional outer mesh has an influence on the focussing of the emitted electron beam. Figures 4.4(b) and 4.4(a) show the equipotential lines obtained in the calculations described above. Two examples illustrating the effect of concave and convex configurations of equipotential lines on the electron trajectories are found in Figure 4.4(c). The right part of the example demonstrates the focussing the effect of a so called Wehnelt cylinder, shown in grey, which has a small negative bias potential with respect to the blue filament. By comparing the equipotential lines obtained from field calculations seen in Figures 4.4(b) and 4.4(a) to these examples, one can estimate how the electric fields affect the width of the emitted electron beam. In the case of a grounded outer mesh the equipotential lines are very similar to those observed for the Wehnelt cylinder

[1] This property of the mesh is exploited in Penning ion sources, where an additional cathode at the same potential as the hot cathode is used to reflect back electrons that have escaped the interaction region [20]

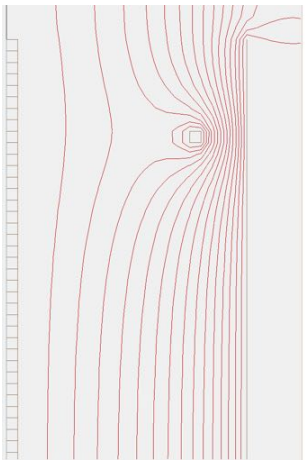

(a) SimIon calculation for $U_{mesh} = 220\,\mathrm{V}$

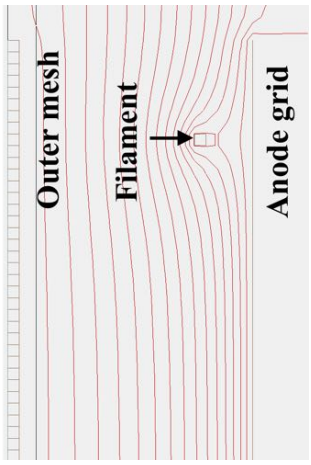

(b) SimIon calculation for $U_{mesh} = 0\,\mathrm{V}$

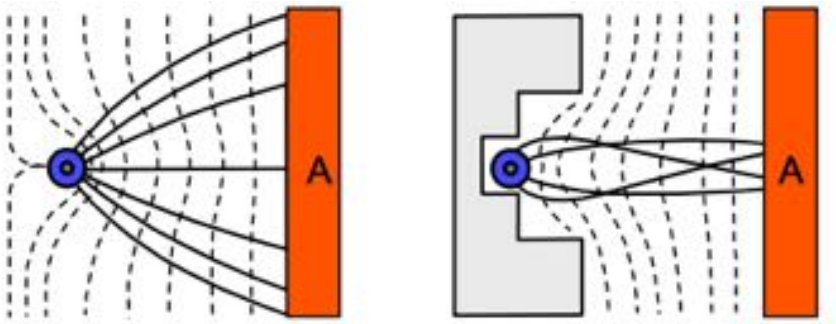

(c) Illustration from [20]

Figure 4.4.: Equipotential lines in space obtained from field calculations in SimIon of the MIRACLS ion source for different mesh voltages. The effect of the distribution of equipotential lines on the electron trajectory is shown in Figure 4.4(c), where A is the anode, the blue circle corresponds to the cathode filament and the grey Wehnelt cylinder is negatively biased with respect to the filament.

implying a focussing property of the electric field configuration. In the case of a bias voltage of 220 V to the outer mesh, no potential bias is present between the mesh and filament and the equipotential lines in Figure 4.4 imply a defocussing of the emitted electron beam.

It can thus be concluded, that even in the total absence of space charges the application of a voltage equal to that of the filament is beneficial for the number of electrons emitted and extracted from the filament and received at the grid.

A potential drawback are the defocussing properties of this potential configuration.

4.1.2. Space-charge considerations

The results of the field calculations presented in the previous Section 4.1.1 were used as the starting point for the formulation of hypotheses regarding the effect of the outer mesh on space-charges. Figure 4.5 illustrates the expected consequences in the presence of space charges in the simplified geometry of a set of parallel plates similar to Figure 3.4. This qualitative representation shows the potential distribution in space as one would expect in the presence of an electron cloud near the cathode. If the outer mesh is grounded, which is similar to the initial configuration of the set-up, calculations indicate, that the filament corresponds to a minimum in potential energy even in the absence of space-charges as shown by the calculations discussed above. The presence of an electron cloud is expected to deepen the potential well at the filament with respect to both sides as shown in Figure 4.5. This increases

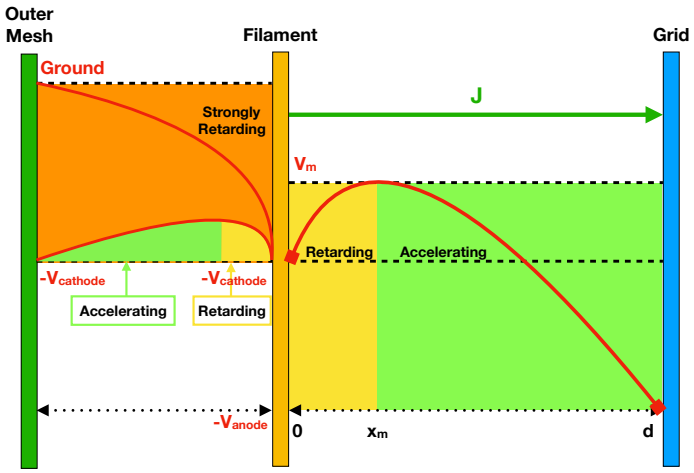

Figure 4.5.: Sketch of the reasoning behind the integration of an additional outer mesh (green), to which a voltage can be applied, into the set-up. The right hand side corresponds to Figure 3.4. The left hand side shows the potential energy distribution for the outer mesh potential set to $U_{mesh} = 0\,\mathrm{V}$ (top red curve) and $U_{mesh} = U_{filament}$ (bottom red curve). Annotations highlight the expected effect on electron trajectories within the region. Created and modified based on [19].

the strength of the electric fields forcing the electrons back towards the filament. Hence, a further decrease in the electrons received by the anode grid is anticipated. The bottom curve on the left hand side of the filament in Figure 4.5 illustrates the effect of biasing the plate to the same voltage as the filament. One may still expect

a retarding region within the space-charge cloud close to the filament. Therefore the formation of a potential maximum at the densest point of the space-charge cloud close to the cathode is anticipated. On the left hand side of this maximum close the outer mesh, the potential would decrease resulting in an accelerating electric field for those electrons that can overcome the potential barrier. The presence of an additional component biased at 220 V would therefore result in a more diffuse and less dense electron cloud surrounding the filament reducing the detrimental effects of space-charges.

In summary, based on the calculations presented in this section, the decrease in current observed in Figure 4.1 can be explained by the formation and deepening of a potential well at the filament due to its positive potential bias voltage.
The addition of an outer mesh biased to a voltage close to, but below that of the filament is expected to significantly increase the electron yield at the grid due to changes in the electric fields at the filaments and the implications of those electric fields on space-charge clouds. The better the grid and filament are shielded from the outer grounded components by means of this mesh, the more independent the electron current becomes from the filament bias voltage. Hence, a large electron current can be maintained, even when $U_{filament} = 220\,\mathrm{V}$. However, this might be accompanied by a defocussing of the electron beam when the bias voltage of the additional component is close to that of the filament.

4.2. Experimental set-up

For an initial first proof-of-concept experiment, only a plate instead of a full mesh was added to the set-up. For simplicity the copper plate used as a Mg dump and for heat transport away from the set-up, was replaced with an aluminium one. The plate was electrically isolated from the rest of the set-up such that an independent electric potential could be applied to it. A side view of the set-up including the aluminium plate is shown in Figure 4.6. The outer mesh later installed in the set-up was built based on a stainless steel grid bent into a cylindrical shape and fixed at point-welded spots. The dimensions were chosen such as to cover as much of the surface surrounding the filament as possible without making electric contact with other source components apart from the previously introduced aluminium plate. Prior to the installation in the ion source set-up, the outer mesh was fixed to the

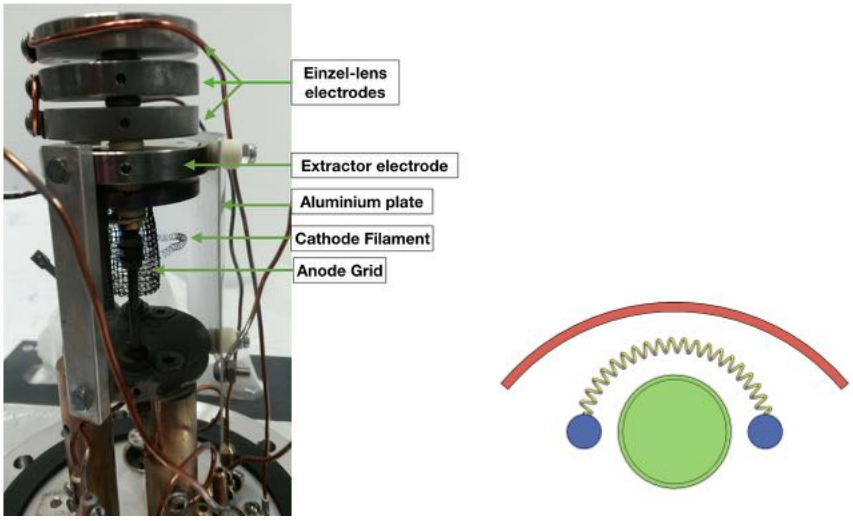

(a) Side view photograph (b) Top view sketch

Figure 4.6.: Side view photograph and top view sketch of MIRACLS' ion source set-up including the newly added aluminium plate (red). The sketch shows the two leads (blue), the helical filament (yellow) and the anode grid (green).

aluminium plate as shown in Figure 4.7(a) using metallic screws such that an electric potential applied to the aluminium plate would also be applied to the entire outer mesh. The complete set-up including the mesh can be seen in Figure 4.7(b). During the tests discussed in the following section, the effect of the bias voltage $U_{plate/mesh}$ applied to the plate or outer mesh as well as the accelerating voltage ΔU, i.e. potential difference between filament and grid, and filament heating power P on the electron currents I were studied. The electron currents of interest in the measurements are those received at the anode grid I_{grid} and the aluminium plate I_{plate} (or mesh I_{mesh}) as indicated in Figure 4.8, as well as the current emitted from the filament I_{total}.[2] The total current I_{total} is given by the sum of the currents I_{grid} and $I_{plate/mesh}$ and was found to be equal to the current emitted from the filament at all times. Values of $U_{grid} = 250\,\mathrm{V}$ and $U_{filament} = 220\,\mathrm{V}$ amounting to an accelerating potential difference of $\Delta U = 30\,\mathrm{V}$ were applied unless indicated otherwise. One or two helical filaments of $\sim 19\,\mathrm{cm}$ length were used. During all tests presented, the Mg oven was removed from the set-up.

[2] At the end of all test presented in this section, selected points of the measurement were repeated in order to identify systematic drifts of the system. These measurement points are plotted alongside the other data points in the respective plots. Errorbars for the currents and voltages applied as well as the measured heating powers are too small to be visible in the plots.

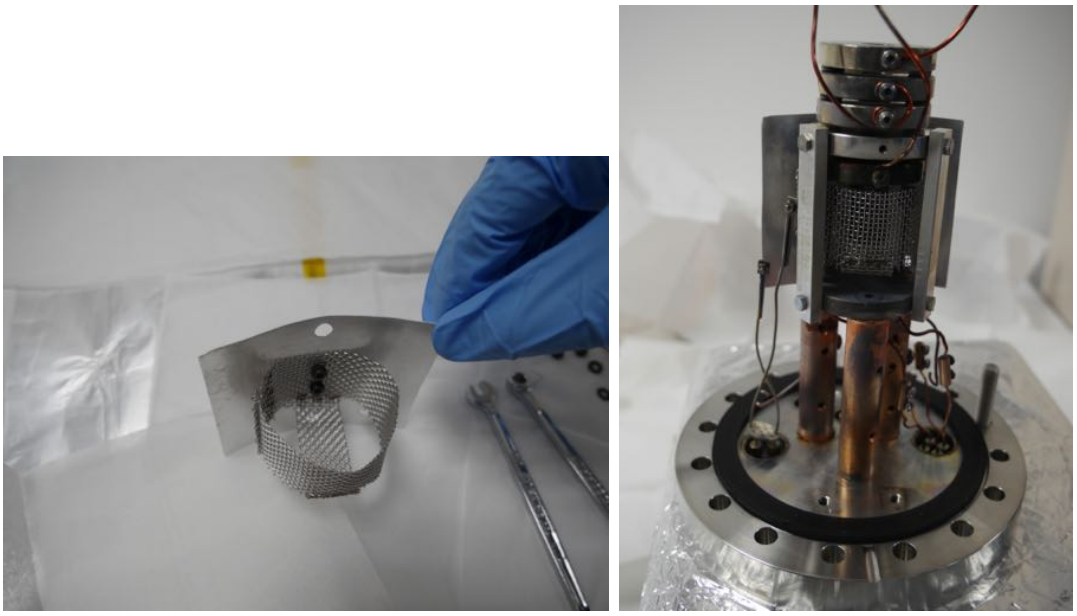

(a) Mesh before installation (b) Mesh installed in the set-up

Figure 4.7.: The additional outer mesh before and after installation in the ion source set-up. Figure 4.7(a) shows the mesh attached to the aluminium plate, in Figure 4.7(b) the full ion source set-up including the mesh can be seen.

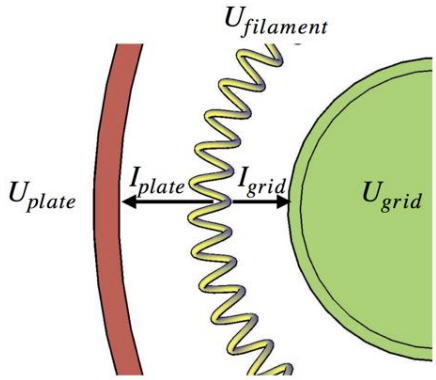

Figure 4.8.: Close up of Figure 4.6(b) including the potentials and currents of interest.

4.3. Experimental results

4.3.1. Aluminium plate

Figure 4.9 shows a first demonstration of the beneficial effect of a positive bias voltage at the aluminium plate on the number of electrons received at the grid.

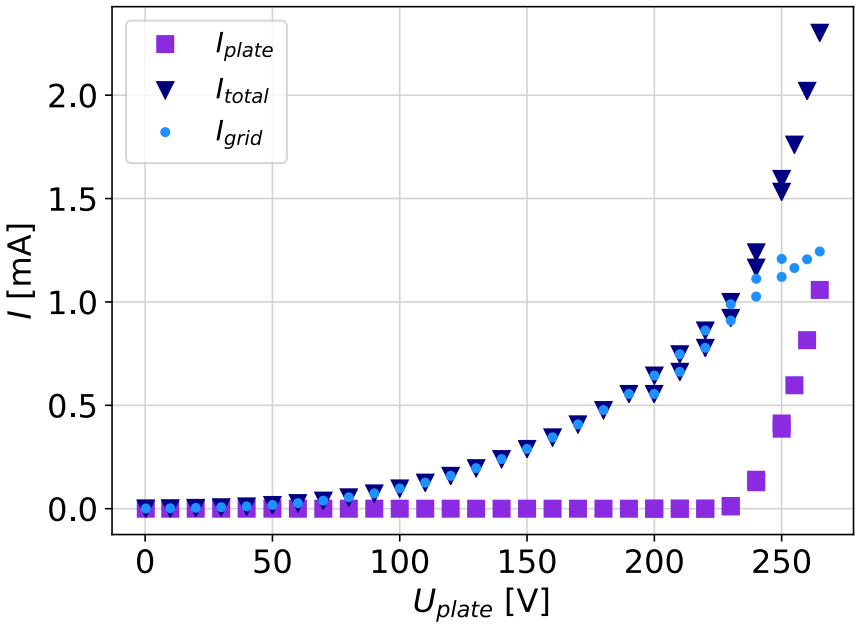

Figure 4.9.: Electron currents received at the grid I_{grid}, the plate I_{plate} and emitted from the filament I_{total} for a filament heating power $P = 35\,\mathrm{W}$ as a function of the bias voltage U_{plate} applied to the Al plate.

The current I_{grid} received at the anode grid, I_{plate} received by the plate and the total current I_{total} emitted by the filament are plotted as a function of the aluminium plate bias voltage U_{plate}. The conditions in the initial set-up including the copper plate corresponds to $U_{plate} = 0\,\mathrm{V}$. The increasingly positive bias voltage of the aluminium plate results in a strong increase of I_{grid} and I_{total}, while no electrons are collected at the Al plate. Only when the plate voltage exceeds the filament voltage, part of the electrons emitted from the filament are accelerated towards the plate resulting in a significant increase in I_{plate}. The collection of electrons at the Al plate is not desirable and in most cases, the onset of I_{plate} caused I_{grid} to plateau and decrease. Therefore the maximum current is obtained for a plate bias voltage close to, but not exceeding $U_{plate} = U_{filament}$. The increase in electron current observed in Figure 4.9 amounts to a factor of 120 when changing U_{plate} from 0 V to 220 V. This exceeds the

effect that can be achieved via the Schottky effect by several orders of magnitude and is thus associated with space-charge effects discussed in Section 4.1.2.
In Figure 4.10 the current I_{grid} as a function of the filament heating power supply floating voltage $U_{filament}$ is shown. The acceleration voltage $\Delta U = U_{grid} - U_{filament}$ is kept constant at 30 V throughout the measurement as required for efficient Mg ionisation. The case of a grounded plate $U_{plate} = 0\,\mathrm{V}$ corresponding to the initial condition in Figure 4.1 is shown in comparison to the case in which the aluminium plate is held at a constant potential difference below the filament voltage. The grid current recorded for the case, in which the aluminium plate bias voltage is varied, exhibits a more gradual decrease and follows an approximately linear trend in $U_{filament}$. The data plotted in Figure 4.10 reveals that for $U_{plate} = 0\,\mathrm{V}$, raising the filament bias voltage from 60 V to the nominal value of 220 V, I_{grid} falls to as little as 1% of its initial value, confirming the expectation regarding the effect of the bias voltage. When the potential difference between plate and filament is kept constant and $U_{plate} = U_{filament} - 30\,\mathrm{V}$, I_{grid} is reduced to 60% of its initial value for the same increase in $U_{filament}$.

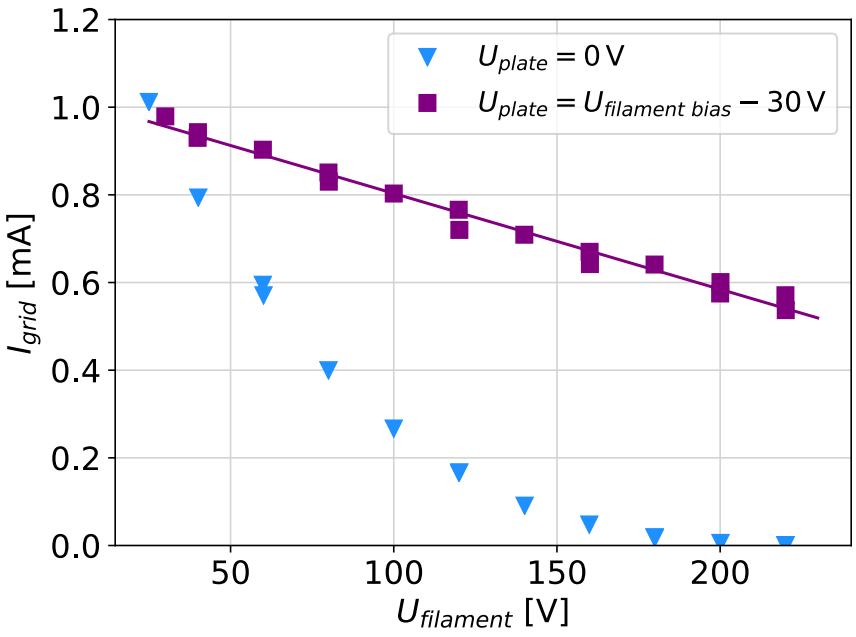

Figure 4.10.: Electron currents I_{grid} received at the grid for a filament heating power $P = 35\,\mathrm{W}$ as a function of the bias voltage $U_{filament}$ applied to the filament for different plate voltages U_{plate}. The solid line corresponds to a linear fit to the data for $U_{plate} = U_{filament} - 30\,\mathrm{V}$.

The aluminium plate therefore has the capability to greatly reduce the undesired effect of a reduced electron current when floating $U_{filament}$ to positive relative potentials.

4.3.2. Addition of an outer mesh

Further improvements are expected with the addition of the outer mesh to the set-up. Figure 4.11 compares the electron currents obtained with the set-up including

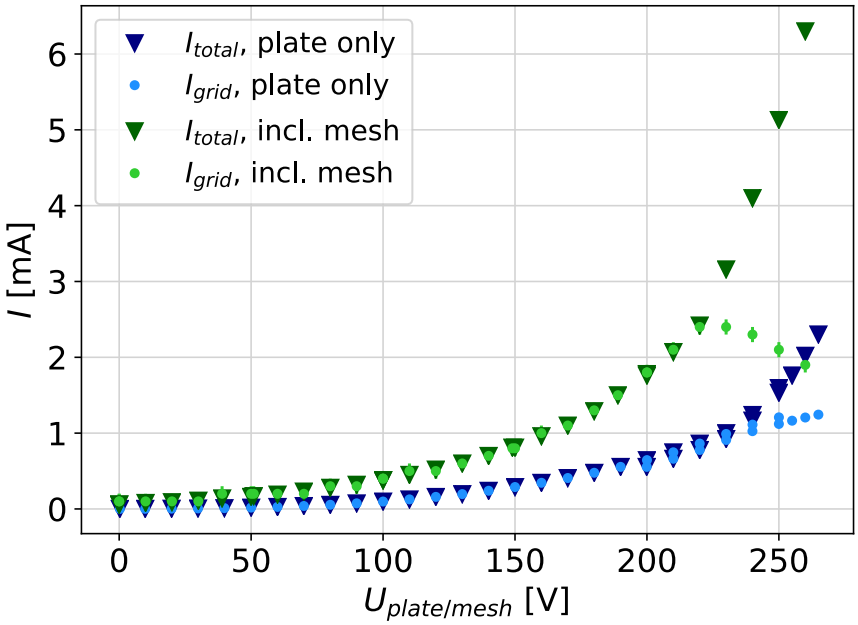

Figure 4.11.: Electron currents received at the grid I_{grid} (dots) and emitted from the filament I_{total} (triangles) for a heating power $P = 35\,\mathrm{W}$ as a function of the bias voltage applied to the plate U_{plate} or mesh U_{mesh}. The set-up contained one long helical filament and either only the aluminium plate or both the plate and the outer mesh.

the mesh with the data shown in Figure 4.9 achieved with the Al plate alone. As expected, the total values of the currents observed with the biased mesh exceed those obtained with the aluminium plate. [3] Figure 4.12 shows data taken in the

[3] It is important to note, that several other factors potentially contributed to some extent to the observed difference between the set-up with and without the mesh. The introduction of the mesh imposed additional constraints on the positioning of the filament. This most likely resulted in an increased proximity between mesh and filament, which as will be shown in Section 5 contributes to an increase in electron current. In addition, small differences between the filament lengths result in slightly different temperatures of the filament for a given heating

same manner as in Figure 4.10 for the set-up including the mesh. When comparing the curve recorded for $U_{mesh} = 0\,\mathrm{V}$ and for $U_{mesh} = U_{filament} - 30\,\mathrm{V}$, again the decrease in the latter is less steep and approximately linear. The linear regression seen in Figure 4.12 yields a slope of $\sim 1.2 \cdot 10^{-3}\,\mathrm{mA/V}$ compared $\sim 2.2 \cdot 10^{-3}\mathrm{mA/V}$ in the case of the plate only. Therefore the undesired reduction in electron emission when floating the filament is even more efficiently reduced using the outer mesh than the plate only. This is a direct consequence if the fact that the shielding from surrounding components at ground potential is superior for a cylindrical mesh surrounding the filament and grid than for a single plate on one side of the setup.

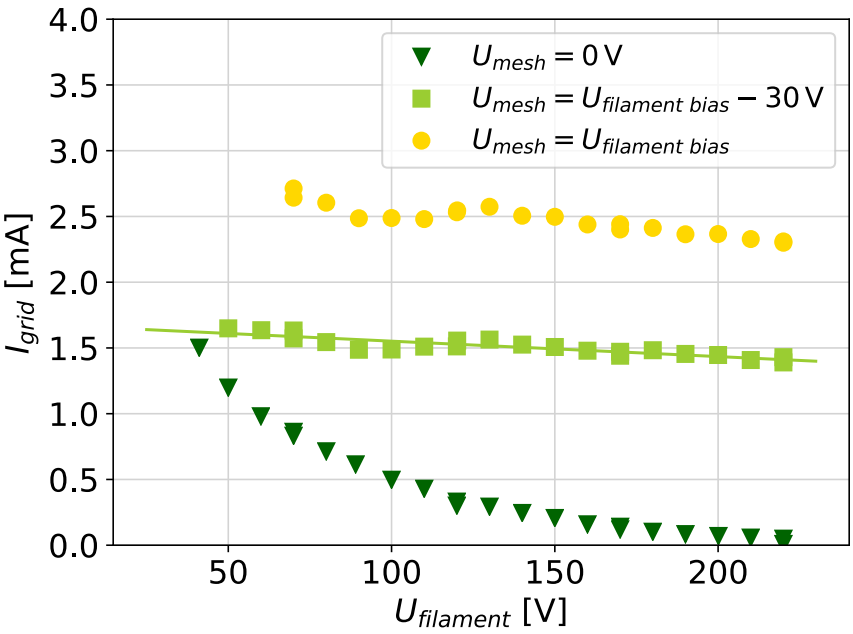

Figure 4.12.: Electron currents received at the grid I_{grid} for a filament heating power of $P = 35\,\mathrm{W}$ as a function of the bias voltage applied to the filament $U_{filament}$ for different plate voltages U_{plate}. The potential difference between the anode grid and the filament bias voltage is kept constant at 30 V. The solid line corresponds to a linear fit to the data for $U_{plate} = U_{filament} - 30\,\mathrm{V}$.

power with shorter filaments resulting in higher currents. This second point is discussed in greater detail in Section 5.3.

Finally, Figure 4.13 presents a logarithmic plot of the current I_{grid} as a function of the electron acceleration voltage $\Delta U = U_{grid} - U_{filament}$ for different fixed values of U_{mesh}. ΔU is varied by increasing U_{grid} with respect to a fixed $U_{filament} = 220\,\mathrm{V}$. For high values of ΔU, transition into the temperature-limited regime takes place, in which the current saturates and only increases very slightly with ΔU due to the Schottky effect. It can be seen in Figure 4.13 that not only does the total current rise with increasing U_{mesh}, but also that the transition to the temperature-limited regime, in which the current as a function of ΔU saturates, is accomplished at smaller values of ΔU. Only for the highest values $U_{plate} = 210\,\mathrm{V}$ and $U_{plate} = 220\,\mathrm{V}$ the full transition is visible in the ΔU interval studied in Figure 4.13. This implies that as sketched in Figure 4.5 the outer mesh counteracts the build-up of space-charge clouds around the filament. This allows to take advantage of even higher heating temperatures of the filament due to the reduction in space-charge effects which would otherwise make the elctron current collected at the grid rather insensitive to an increase in filament temperature.

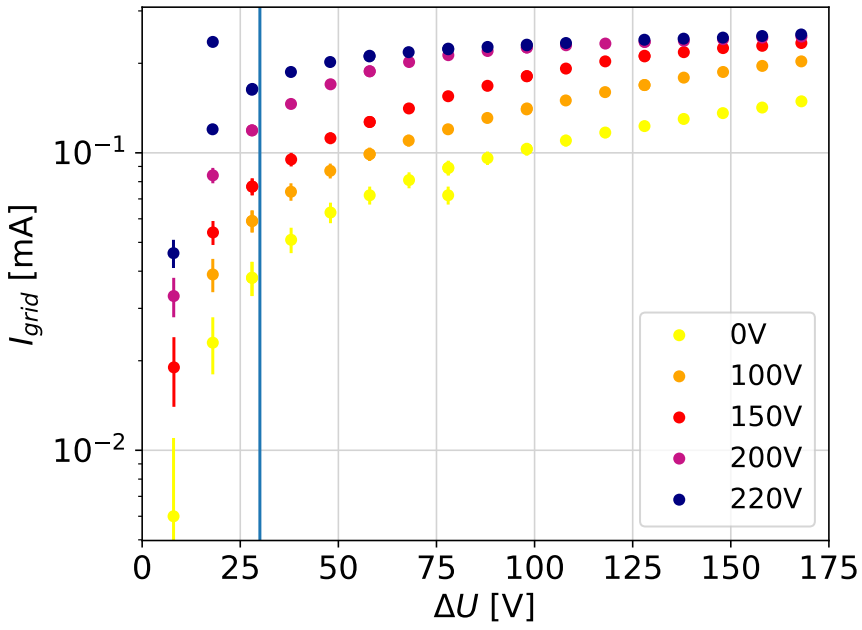

Figure 4.13.: Electron currents received at the grid I_{grid} for a heating power $P = 40\,\mathrm{W}$ as a function of the accelerating potential difference ΔU between anode grid and cathode filament. The filament voltage is fixed at $U_{filament} = 220\,\mathrm{V}$ and U_{grid} is varied. different values for U_{mesh}. The vertical blue line indicates the value of $\Delta U = 30\,\mathrm{V}$ used in the MIRACLS set-up.

5. Optimisation of filament parameters

The filament radius, length and position can be identified as the parameters of potential significance to the electron rates obtained from a filament within MIRACLS' ion source. In addition to the total electron currents, the filament parameters also affect the heating efficiency of the filament, that is the filament temperature obtained for a given heating power. As restricting the heating power to low values is critical for extending the life-time of the MIRACLS ion source, increasing the heating efficiency is highly desirable and modifications yielding increases in the current have to undergo careful assessments of potential drawbacks with regards to increases in the required heating power. The first part of this chapter discusses the optimal values of the filament parameters based on theoretical calculations including both the temperature and the space-charge-limited regime. The changes that were introduced in the ion source set-up motivated by these calculations are presented in the second part, followed by the experimental results obtained with the modified configurations.

5.1. Calculations based on theory

Theoretical expectations concerning the impact of filament parameters on the obtained electron current vary greatly based on whether the cathode is operating in the temperature or the space-charge-limited regime. As discussed in Section 3.2, operation in the transition region between the two regimes is often desirable. Hence, the effect of the filament parameters in both regimes is of interest in MIRACLS' ion source. In general the total current I at the anode depends on the surface area A of the filament and thus on its radius r and length l according to

$$I = J \cdot A = J \cdot 2\pi l r. \tag{5.1}$$

The total current thus increases with filament length and radius. While the current *density* emitted from the filament surface is independent of filament dimensions, the filament length and radius have an impact on the heating efficiency as well as the presence of geometry-dependent space-charge clouds. In the space-charge-limited regime electrons escape from the edge of the space-charge cloud and therefore one would expect the surface of the corresponding space-charge-cloud to play a significant role in addition to the surface of the filament. The idea behind this is illustrated in Figure 5.1. Whilst the surface of a helically shaped filament is much larger than that of a straight filament, the space-charge cloud is not increased by the same factor, such that Equation 5.1 does not necessarily hold in the space-charge-limited regime. [1]

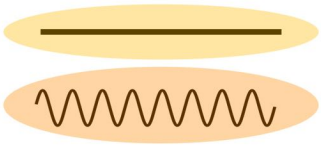

Figure 5.1.: Sketch of the reasoning behind choice of the filament shape. A short, straight and a longer, helical filament are shown and their space-charge clouds indicated.

The straight filaments are much shorter than helical ones which corresponds to a much smaller surface from which the electron emission occurs with a given current density. In MIRACLS' ion source set-up, straight filaments are between 3.5 and 5 cm long, while helical wires can easily reach lengths of about 20 cm. This corresponds to a increase in the surface by about a factor of ~ 5. However, one would expect the space-charge clouds surrounding the helical filament to be much denser as the points from which electrons are emitted are in increased proximity of one another in comparison to the straight filament. Therefore the cloud would be already denser at lower temperatures resulting in the onset of the transition to the space-charge-limited regime at lower temperatures. The space-charge cloud probably also trap electrons emitted into the inner region of the helix and prevents them from contributing significantly to the currents at the anode. Electrons emitted on the far side of the filament with respect to the anode grid also

[1] Finally, calculations of the magnetic field strength for the straight and helical filaments show that the magnetic fields expected for the filament currents used in the MIRACLS ion source are at most in the order of a few percent of the earth magnetic field in both cases and thus negligible.

experience significant shielding from the accelerating electric field. Based on these considerations, one might disfavour longer filaments in a helical structure, despite their greater surface.

In the temperature-limited regime, which is of interest mostly if straight filaments are employed, the filament's length and radius profoundly affect the heating efficiency. The following calculations of the effect of the filament parameters are based on the assumption, that the electric heating power $P_E = I_H^2 R$, where R is the resistance and I_H is the heating current, is equal to the power P_H radiated by the filament at temperature T according to the Stefan-Boltzmann law

$$P_H = 2\pi\epsilon\sigma T^4 r l, \tag{5.2}$$

where ϵ is the emissivity of the filament material and σ is the Stefan-Boltzmann constant. This approach neglects the power losses by thermal conduction and electron emission and heating powers required in experiments will slightly exceed the values obtained from Equation 5.2. The heating power required to reach a given temperature in Equation 5.2 increases linearly with r and l. Solving Equation 5.2 for T and plugging it into the Richardson equation 3.2 yields the current I emitted from the filament for a fixed heating power as a function of filament radius r and length l. Figure 5.2 displays the total current that can be obtained for a constant heating power of 20 W for the case of pure as well as thoriated tungsten filaments. For a constant heating power the dependency of the emitted current I on the parameters r and l is very different from Equation 5.1. The emitted current increases for shorter and thinner filaments as heating becomes more efficient and higher temperatures can be reached for a given P. When combining the results presented in Figure 5.2 with the discussions above regarding the space-charge-limited regime, shorter, straight filaments appear to the better choice for MIRACLS' ion source as they delay the onset of space-charge effects to higher temperatures, which according to Figure 5.2 can be reached at lower heating powers for shorter filaments.

A decrease in the radius whilst beneficial for heating efficiency, is expected to make the wire even more brittle and could lead to problems with its installation. For this reason as well as the fact, that only small changes in the current can be obtained for a reasonably smaller radius, switching to thinner wires is deemed unfeasible for the ion source set-up.

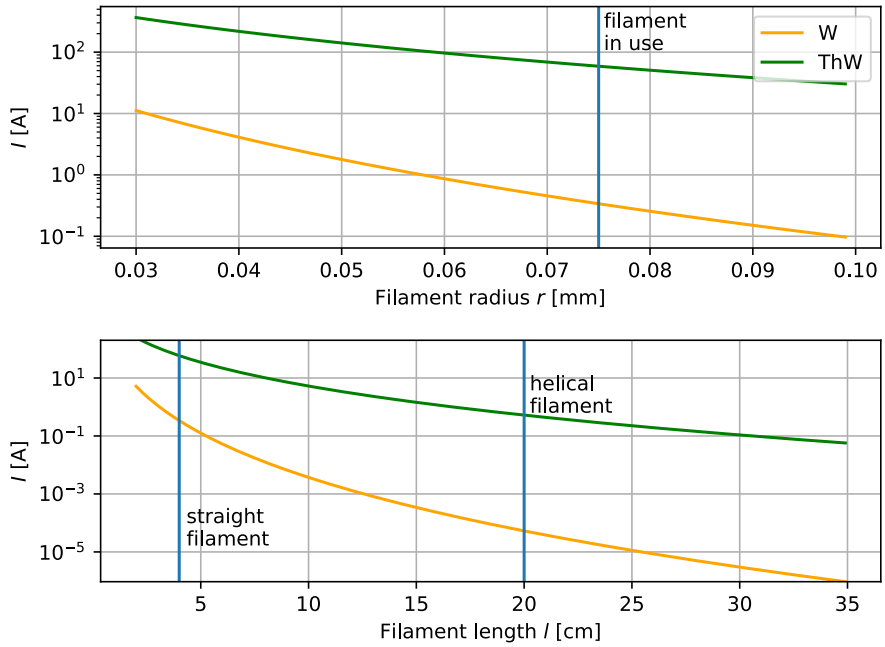

Figure 5.2.: Emitted electron current I for a given filament heating power $P = 20\,\mathrm{W}$ as a function of filament radius r and length l respectively. Typical filament lengths and the radius in use at the MIRACLS' ion source are indicated by vertical lines. For the upper plot, the filament radius in use at MIRACLS' ion source of $r = 0.075\,\mathrm{mm}$ was used in calculations. The filament length was set to $l = 4\,\mathrm{cm}$ for the lower plot. Choosing different values of l for plotting were not found to result in significant changes in the shape of the curve.

The final parameters that influence the electron currents obtained are the position and shape of the filament with respect to the other components of the ion source. Apart from the Schottky effect, these two factors are of interest in the space-charge-limited regime only, where the electric fields acting on the electrons are of crucial importance. As discussed above, the two practical options for the filament shapes are straight and helical, the latter of which has already been described to be rather detrimental when it comes to space-charge effects. The position which is inextricably linked to the geometry of the filament determines the electric field strength at the filament. As seen for the case of two parallel plates in Section 3.2, the electric field strength $E = \frac{\Delta U}{d}$ increases with decreasing distance d between the two plates. According to Equation 3.4, the current density J for this geometry rises with $\frac{1}{d^2}$. Qualitatively, the same is true for the case of the grid anode and the filament, albeit the exact nature of the correlation may be more complex. As increased electric fields

strength also slightly increase the emission rates in the temperature-limited regime due to the Schottky effect, no drawbacks are expected from reducing the distance between filament and anode grid, as long as no contact or electrical sparking is established during operation.
In summary, straight, short filaments placed close to the anode grid whilst avoiding contact between the two are expected to yield the optimal electron emission efficiency for MIRACLS' ion source, where the filament heating power should be minimised whilst maximising the number of electrons available for Mg ionisation.

5.2. Experimental procedures

The observable of interest is as in all studies the current received by the grid, the plate and that emitted from the filament. Different values for the parameters discussed above were used in the measurements in order to study their effect on these currents. Figures 5.3(a) and 5.3(b) show the different positions of the long filaments studied. Figure 5.3(b) corresponds to a smaller distance d between anode grid and cathode filament than 5.3(a). Figure 5.4 displays a short filament of about $4-5\,\mathrm{cm}$

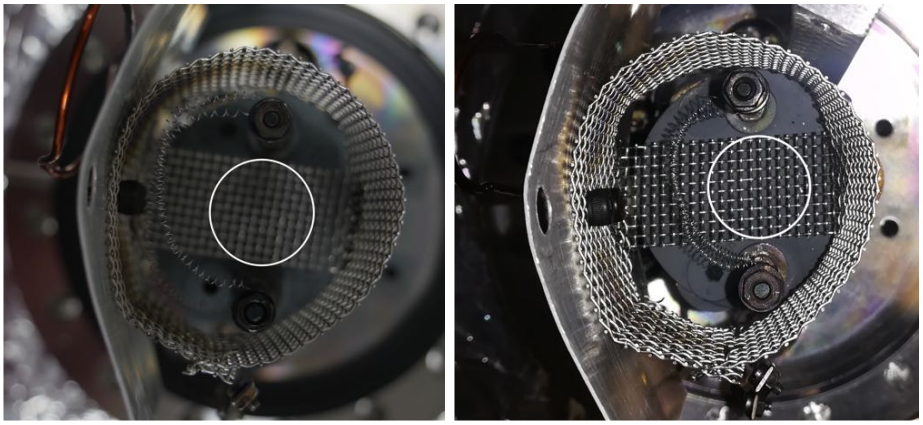

(a) Filament position before move (b) Filament position after move

Figure 5.3.: Position of two long filaments in the ion source set-up before and after increasing the proximity between the filaments and the anode grid, the position of which is approximately given by the white circle. The M3 nuts at the leads give an idea of the absolute set-up dimensions.

length installed in the set-up. In comparison to Figure 5.3(b) it is also important to note, that the filament is even closer to the anode grid in this case. In addition to these changes of the filament shape and position, different numbers of filaments

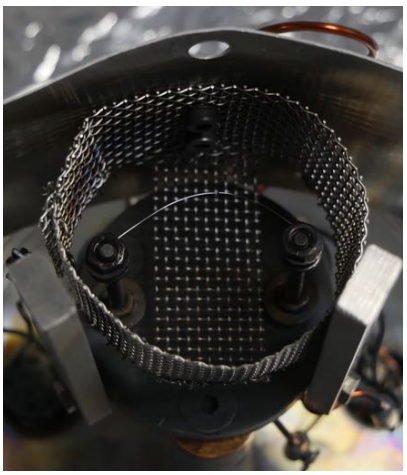

Figure 5.4.: Straight filament in the ion source set-up.

were used. When long, helical filaments were employed, both were placed on the side facing the aluminium plate, while two short, straight wires were placed on opposite sites such as to form a circle around the anode grid. In both cases the exact length and position of the filaments was not easily reproducible after filament exchange. This has pronounced effects, acoording to the $1/d^2$ dependence in Child's law 3.4. Values of $U_{grid} = 250\,\mathrm{V}$ and $U_{filament} = 220\,\mathrm{V}$ amounting to an accelerating potential difference of 30 V were used unless indicated otherwise. During all tests presented, the Mg oven was removed from the set-up.

5.3. Experimental results

In Figure 5.5 the measured electron current I_{grid} is plotted as a function of the heating power P for the two different filament positions shown in Figure 5.3. While two filaments were used in both cases, the filaments were replaced and installed significantly closer to the grid in the second set of measurements. The overall shape of the two curves in Figure 5.5 strongly resembles that of seen in Figure 3.5 as expected due to the heating power being a direct indicator of filament temperature. For low heating temperatures, the current received by the grid is temperature-limited and therefore nearly independent of the filament position and U_{mesh}. The filaments currents only differ for P above about 35 W, where space-charge effects gain importance. As the filament temperature and thus the density of the space-charge cloud rises, the difference in I_{grid} for the two filament positions increases as well. Similar to the case shown in Figure 4.13, the reduction in space-charge effects does not only

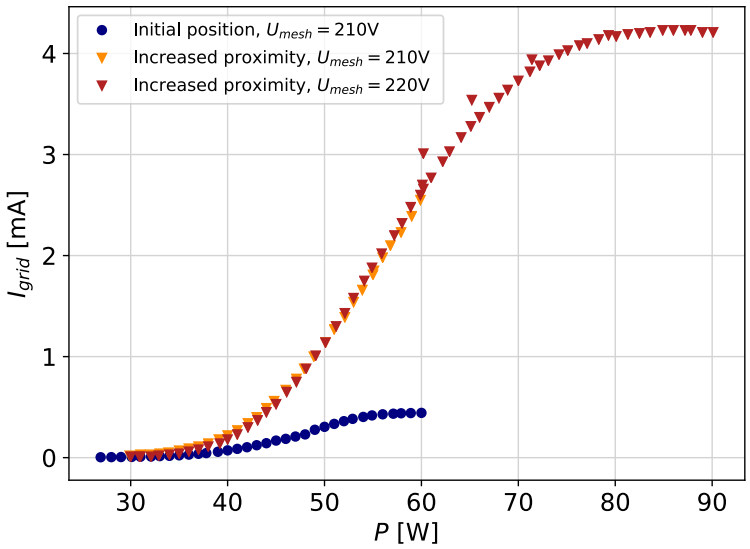

Figure 5.5.: Emitted electron current I_{grid} as a function of filament heating power P for two different filament positions in different proximity to the anode grid and different values of U_{mesh}.

result in higher currents for a given temperature in the space-charge-limited regime, but also in a later onset of the transition to the fully space-charge-limited regime; I_{grid} saturates at much lower heating power for the filament further away from the grid. A decrease in distance d between grid and filament thus does not only yield higher currents for a given heating power, but also greatly enhances the maximum current that can be obtained in the fully space-charge-limited regime, by shifting the transition temperature similar to observations found in the literature and seen in Figure 3.5.

The difference between the two data sets recorded for different U_{mesh} also emerges at high temperatures and is due to space-charge effects. The effect of the mesh potential U_{mesh} on electron currents is discussed in detail in chapter 4.

Figure 5.6 compares the currents obtained for two different filament lengths and corresponding shapes. I_{grid} is plotted as a function of the mesh bias voltage U_{mesh} for a long, helical filament of about 19 cm length for heating powers of 25 W and 50 W and for two short, straight filaments of $4 - 5$ cm heated with a total heating power of 20 W. The overall shape of the curve appears to be independent of filament number and length as well as heating power. For a shorter filament, heating is much more efficient. This appears to be confirmed by the observation, that the

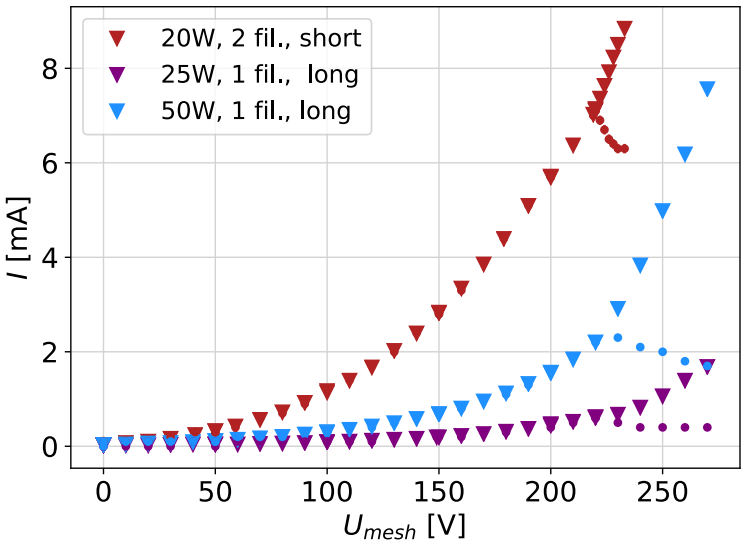

Figure 5.6.: Emitted electron current I_{total} (triangles) and current to the grid I_{grid} (dots) as a function of the bias voltage U_{mesh} applied to the mesh for different filament lengths and numbers.

maximum value of $I_{grid} = 3.5\,\text{mA}$ per short filament at 10 W [2] per filament exceeds the maximum $I_{grid} = 2.2\,\text{mA}$ obtained in the case of a single long helical filament at 50 W. The length of the short filament only amounts to about $\frac{1}{5}$ of that of the long, helical filament and it is heated by 10 W corresponding to $\frac{1}{5}$ of the heating power used in the long filament, such that the heating power per filament length is approximately equal in both cases. As this indicates similar filament temperatures, the excess current in the case of the straight filament is likely caused by a reduction in space-charge density confirming the hypothesis for the filament shape as discussed in Section 5.1.

Therefore, in the general case, the total increase in electron current obtained for a given total filament heating power by switching from a long, helical filaments to a short, straight ones is interpreted to be due to a combination of the increase in temperature due to the increased heating efficiency as well as the reduction in space-charge effects discussed in Section 5.1.

Figure 5.7 and Figure 5.8 show studies concerning the number of filaments used. In both cases short filaments of about 5 cm length are utilised, although length may

[2] 7.0 mA were measured for 20 W for two filaments. Due to the parallel circuit configuration of the filaments, each is heated by half of the total power. Assuming approximately equal dimensions for both filaments, each is expected to contribute half of the observed electron current

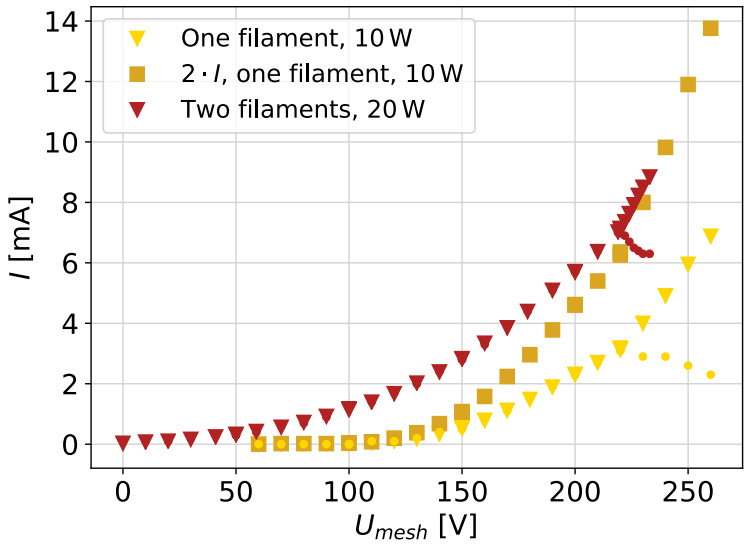

Figure 5.7.: Electron current emitted from the filament I_{total} (triangles) and current I_{grid} received by the grid (dots) as a function of the bias voltage U_{mesh} applied to the outer mesh for different filament length and numbers.

vary by several mm between individual filaments.

Figure 5.7 shows I_{grid} and I_{total} as a function of the bias voltage applied to the outer mesh for two filaments on opposite sides of the grid or one filament on the grid side facing the aluminium plate. For better comparison, $2 \cdot I_{grid}$ is shown for the case in which one filament is present in the set-up. The heating power amounts to 10 W per filament in both cases. At similar temperatures, one would expect the relation $I_{2\text{ filaments, }20\,\text{W}} = 2 \cdot I_{1\text{ filament, }10\,\text{W}}$ to hold at least in the temperature-limited regime due to the increase in the emitting surface.

Indeed, as can be seen in Figure 5.7, for high values of U_{mesh} doubling the number of filaments corresponds to an increase by a factor two in the grid current.

Contrary to expectations, for low values of U_{mesh} the current of a single filament is found to be significantly below half of the value recorded for two filaments. This is most likely due to the presence of space-charge-effects. Geometrical factors such as the exact distance between filament(s) and grid are difficult to reproduce when switching between different filament configurations, leading to sizeable differences in the electric field and hence, as discussed briefly in Section 5.2, in the observed electron currents in the space-charge-limited regime. Moreover space-charge effects might be enhanced for two filaments, as the distance between the two filaments becomes very small close to the points at which they are fixed to the leads. This

might result in an overlap of space-charge clouds. An additional factor might be the less pronounced cooling of the filament due to the cold leads caused by the presence of two hot filaments. Hence, the temperature of the ends of the filaments might differ for two filaments even if each filament is heated by the same heating power, changing their emissive behaviour.

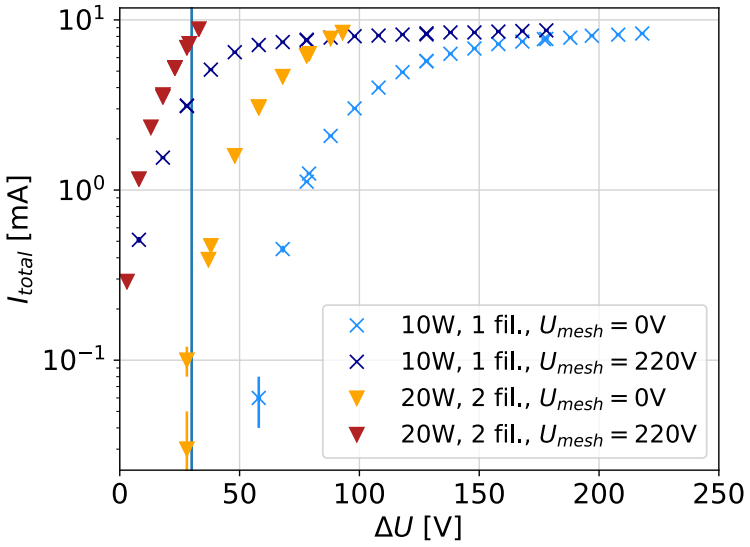

Figure 5.8.: Emitted electron current I_{total} as a function of the accelerating potential difference ΔU between anode grid and cathode filaments for one or two short filaments and different values for U_{mesh}. The vertical blue line indicates the value of $\Delta U = 30\,\mathrm{V}$ used for the MIRACLS set-up. ΔU in varied by changing the grid potential U_{grid} whilst fixing the filament potential at $U_{filament} = 220\,\mathrm{V}$.

Figure 5.8 sheds more light into the question for the cause of the unexpected discrepancy between the electron currents observed for different numbers of filaments in Figure 5.6 at low U_{mesh}. By studying the grid current as a function of $\Delta U = U_{grid} - U_{filament}$, it is possible to determine whether the filaments are operating in the temperature or space-charge-limited regime. It can be seen that for the potential difference ΔU of 30 V studied in Figure 5.7 and indicated by a vertical line in Figure 5.8, the two-filaments configuration is more severely space-charge-limited and farther away from saturation than in the case of one filament. Extrapolating from the data points shown in Figure 5.8, one would expect a significantly higher saturation voltage for the temperature-limited regime in the case of two wires. This is expected due to the doubling of the emitting surface. This however does not explain the shift further into the space-charge-limited regime, which is discusses above.

The more significant increase of the electron current with U_{mesh} for two filaments therefore strongly hints to being more severely space-charge-limited. This increase in space-charge effects can be explained by the aforementioned overlapping and interaction of space-charge clouds as well as changes in filament length affecting positioning and temperature.

In summary, theoretical calculation, indicating that optimal results with respect to electron currents and heating efficiency are obtained with short straight filaments close to the grid, have been confirmed by experiments. The electron current can be boosted further by increasing the number of filaments, provided that the heating power per filament is sufficiently low.

6. The Activation Process

In all measurements presented in Chapters 4 and 5 the thermionic emission properties of the filament were found to correspond to those expected for pure tungsten. As introduced in Section 3.4, a special activation process is required in order to take advantage of the superior emissive properties of thoriated tungsten.
In this chapter the activation process is studied in the MIRACLS ion source set-up. Previous findings regarding the activation are briefly discussed in Section 6.1. This is followed by an overview over the different experimental approaches that were attempted to achieve filament activation for this Bachelor project in Section 6.2 and the subsequent discussion of the results of these approaches.

6.1. Previous results

Experimental evidence for successful activation has been found once in previous work on the MIRACLS ion source set-up [12], see Figure 6.1. The increase in current over time seen in this data is very similar in shape to those found in the literature such as Figure 3.8 suggesting that an activation of the filament took place. However, the data shows an extremely long duration of the activation process amounting to two entire days, which is in contrast to the activation processes described in the literature, where saturation typically sets in after less than one hour. Moreover, the process could not be reproduced after replacement of the filaments. Hence, the necessary procedure and conditions remained unclear. Following in-depth studies of literature on the operation of thoriated tungsten cathodes as presented in Section 3.4, critical parameters and procedures are now identified. These aid the goal of successfully and reproducibly achieving activation of the filament in MIRACLS' ion source.

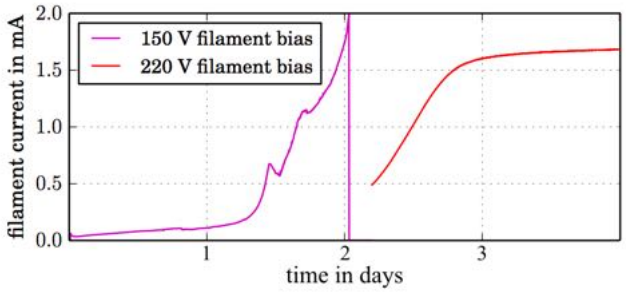

Figure 6.1.: Filament grid current as a function of the duration of the filament conditioning in days during previous work. A rise in current is visible after approximately one day and takes two days to reach saturation. This rise could be interpreted as the onset of an activation process of the filament [12].

6.2. Experimental procedure and results

In order to achieve activation, a number of different approaches described in the publications discussed in Section 3.4 were attempted. The two main steps of the activation process are summarised once more in Table 6.1. First, the filament was operated at activation temperatures between $2000 - 2100\,\mathrm{K}$ for $15 - 20\,\mathrm{min}$. If no activation was observed, the filament was flashed at temperatures exceeding $2800\,\mathrm{K}$ for $3\,\mathrm{min}$ and the first step was repeated. The filament temperature is calculated from the change in filament resistance as described in appendix A.

Step name	Flashing	Activation
Temperatures	$2800\,\mathrm{K}$	$1900 - 2100\,\mathrm{K}$
Duration	$3\,\mathrm{min}$	$15 - 30\,\mathrm{min}$
Effect	Reduction of ThO_2 to metallic Th	Accumulation of Th at the filament surface

Table 6.1.: Overview of the details of the two steps of the activation process.

A significant increase in the current over time was observed at several points during the trials for activation of the filament. However, it was immediately followed by a decrease indicating a deactivation process. In the absence of the Mg oven, no attempt resulted in lasting activation of the filament, despite a wide range of activation temperatures being tested. The reason for this behaviour in contrast to what is reported in the literature remains ambiguous. Scanning electron microscopy observations of the cross section of the filament confirmed the presence of thorium

in the wire in the form of globules. The surface of used and new filaments were studied with energy-dispersive X-ray spectroscopy. The surface compositions showed no indications of carburisation of the filament, which can therefore be excluded as an explanation for the absence of activation [32]. Persistent and reproducible activation was readily observed in the case in which the Mg oven was installed and heated. Here, the Mg vapour in the set-up seems to protect the thoriated tungsten wire from deactivation and the Mg^+ ions might also increase the sputtering away of contaminants on the filament surface, as discussed in Section 3.4. In the absence of Mg, residual oxygen oxidises the thorium at the surface of the tungsten wire resulting in deactivation. This may indicate the presence of too much residual oxygen in the vacuum chamber, despite vacuum pressures in the order of $1 \cdot 10^{-7}$ mbar constituting a significant improvement with respect to the pressures typically reported in the literature.

In all measurements discussed below, two short filaments of ~ 4 cm length, were installed on opposite sides of the grid. The applied voltages amounted to $U_{grid} = 250$ V, $U_{filament} = 220$ V and $U_{mesh} \simeq 220$ V. The temperature of the Mg oven was measured by a thermocouple placed next to the Mg oven.

When the Mg oven was heated by the filament only, temperatures did not exceed $\sim 50\,^{\circ}$C, even after flashing the filament with a total heating power of 45 W, corresponding to a temperature of ~ 2800 K. In the case in which the magnesium oven heating was turned on, the biggest changes in the oven temperature were again observed during and directly following the flashing process. Ramping up the heating power from about 5 W to flashing temperatures at more than 40 W for 3 min increased the temperature by less than ~ 10 K. At Mg oven operating temperatures of ~ 540 K, the effect of the filament heating on the oven temperature is therefore very small.

Figure 6.2 shows the grid currents observed before and at two points in time after the activation process as a function of the filament temperature. The theoretical expectations for pure and thoriated tungsten as seen in Figure 3.6 are plotted for comparison. The data recorded before activation is in good agreement with the expectation for pure tungsten. This is expected for a deactivated filament, in which little metallic thorium is present at the surface. A potential slight gain in grid currents in comparison to pure tungsten is likely due to a very small partial activation that occurred during the ramping up of the filament heating necessary for these measurements.

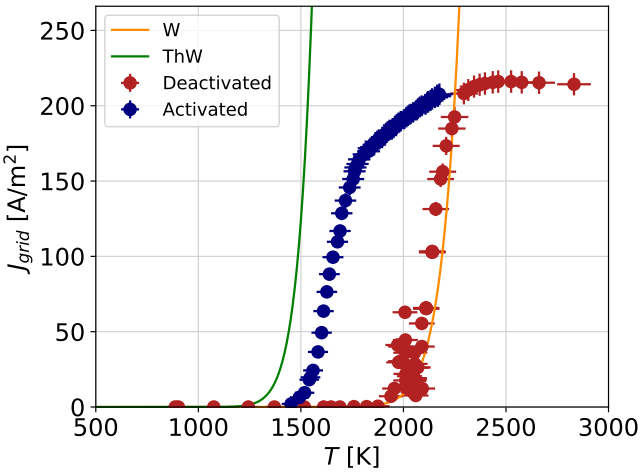

(a) Immediately after activation

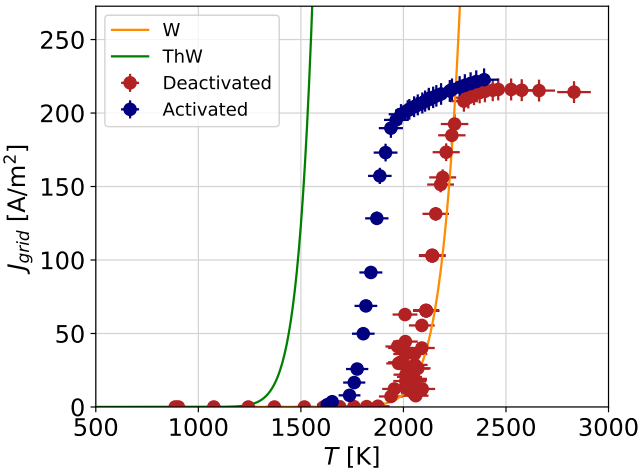

(b) Following operation at 17 W overnight

Figure 6.2.: Current density received at the grid as a function of filament temperature before activation and at two different point in time after activation. The expected current densities calculated from the Richardson equation for pure (W) and thoriated tungsten (ThW) are plotted for comparison.

The saturation at high temperatures corresponds to the transition into the fully space-charge-limited regime, as discussed in previous chapters. After activation, the curve is shifted to lower temperatures corresponding to a decrease of the work function. The overall shape as well as the saturation current is very similar before and after activation. This is to be expected as the space-charge-limited current is independent of the filament work function and only depends on the fixed geometry and voltages. The overall shape of the curves are in good agreement with the shape

of transitions from the temperature- to the space-charge-limited regime found in the literature such as Figure 3.5.
In both Figures 6.2(a) and 6.2(b), the thermionic properties of the filament after activation lie in between those of pure and thoriated tungsten, indicating that only a partial thoriation of the filament took place. This is not surprising as activation times did not exceed 15 min and are thus below the duration of 30 min frequently quoted for activation. Comparing Figures 6.2(a) and 6.2(b) it appears that prolonged filament operation at $P = 17\,\mathrm{W}$ (corresponding to a temperature of $\sim 2150\,\mathrm{K}$) results in a slow deactivation of the filament. This is in agreement with the fact that even temperatures of 2100 K have been reported to lead to deactivation in [38].
In order to compare the emission capabilities of the filament under different conditions, reference measurements at low test temperatures at which no activation or deactivation is expected were conducted. The measurements were performed once after deactivation, once after flashing, and for two activation processes in order to investigate the change in electron current at a given temperature. The values recorded for the grid current can be found in Table 6.2.

Heating		I_{grid} **[mA] for different filament conditions**			
P [W]	T [K]	Deactivated	Flashed	Activated (A)	Activated (B)
4	1650	0.00	0.00	3.01	0.46
5	1720	0.01	0.01	5.03	1.71
6	1770	0.03	0.04	6.14	3.64

Table 6.2.: Grid currents I_{grid} in mA measured at reference temperatures T following different heat treatments of the filament. Conditions A and B as given in the text.

In condition (A), the filament was flashed for three minutes and then activated for 12 min at 2000 K with a nominal $\Delta U = 30\,\mathrm{V}$. In condition B the filament was activated for 10 min at 2000 K with no accelerating voltage $\Delta U = 0\,\mathrm{V}$ between grid and filament after flashing. In condition (B) no ion bombardment of the filament took place during activation due to the absence of an accelerating voltage. As expected, currents are very small after deactivation and flashing, indicating that thorium layer on the surface was nearly completely evaporated. At a testing heating power of 5 W both activation processes yield an increase in current by two orders of magnitude

with the value obtained under condition (A) exceeding the current recorded for condition (B) by more than a factor of 2. The slight difference in activation time is seen as not enough to explain the difference between the two conditions. The comparison between the results obtained after the two different activation processes (A) and (B) could therefore indicate, that whilst activation does occur following a heat treatment alone, positive ion bombardment appears to further boost the process.
After the activation under the conditions given by (B), a further increase in current by about 2 mA up to 4.03 mA for 5 W was recorded following additional activation at 2000 K for 5 min with an applied acceleration voltage of 30 V. The additional rise in current that was observed for activation with ion bombardment after an activation period of 5 min therefore exceeds the rise in current initially achieved with activation at similar temperatures without ion bombardment for 10 min supporting the interpretation that the filament benefits from ion bombardment during activation.
Activation at temperatures of about ~ 2000 K has been found to reproducibly increase currents obtained at low temperatures < 1900 K by two orders of magnitude and was achieved with and without ion bombardment of the cathode. The transition to the space-charge limited regime is shifted to significantly lower temperatures improving heating efficiency. For stable operation, the filament temperatures should not exceed $1800 - 1900$ K corresponding to heating powers of $7.5 - 8.5$ W in this set-up. For an activated filament, this corresponds to operation well within the transition region from the temperature- to the space-charge limited regime.

7. Conclusion and Outlook

This Bachelor thesis contributed to the MIRACLS project which is currently being set up at the radioactive ion beam facility ISOLDE at CERN. MIRACLS utilises a novel approach to collinear laser spectroscopy (CLS) with the potential to overcome the limitations of conventional CLS by employing an MR-ToF device to increase the interaction time between the laser and the radioactive ion beam. This is expected to enhance the sensitivity of the method by up to several orders of magnitude. A proof-of principle experiment, demonstrating the feasibility of this approach, is currently being set up at CERN. For conclusive testing and benchmarking of the experimental set-up as well as the method itself, a reliable offline ion source delivering stable beams of high current over extended periods of time is required.

The goal of this thesis was to increase the lifetime and improve the electron currents in an existing Mg^+ electron impact ion source. Several factors limiting the efficient heating and electron currents flowing between cathode and anode have been identified: the positive bias of the cathode filament, the emissive properties of the filament and the omnipresence of space-charge effects as well as the thermal coupling of the source's Mg oven to the electron emitting filament for operation at high filament heating powers.

The presented work has demonstrated that reducing the positive bias of the filament with respect to its surroundings by applying a voltage close to that of the filament to an external mesh increases the electron current received by the anode grid by up to two orders of magnitude. Different modifications of filament parameters and their implications for heating efficiency and electron currents have been investigated. Two short, straight thoriated tungsten filaments positioned as close to the grid as possible have been found to yield optimal electron currents at significantly improved filament heating efficiencies.

The effect of changing the filament work function by taking advantage of an activation process was successfully demonstrated when Mg vapour was present in the set-up. Filament activation was shown to yield another gain in electron current by two orders of magnitude at low temperatures.
The best results obtained previous to this thesis amounted to $1.7\,\mathrm{mA}/40\,\mathrm{W} = 0.04\,\mathrm{mA/W}$. Combining the modifications briefly described above, this value has been increased to $8.4\,\mathrm{mA}/30\,\mathrm{W} = 0.3\,\mathrm{mA/W}$ in the fully space-charge-limited regime and as much as $6.1\,\mathrm{mA}/5\,\mathrm{W} = 1.0\,\mathrm{mA/W}$ by taking advantage of the filament activation at low operating temperatures. Depending on the mode of operation, this amounts to an increase by one or two orders of magnitude in the currents obtained per W of heating power power whilst also increasing the total electron current by factors of about 3 and 5 respectively.
The impact of the filament heating on the oven temperature in the modified set-up has been shown to be below 10 K at oven temperatures of about 540 K enabling a significantly better and filament-independent control over oven temperatures.
Two modes of operation can be envisioned for the MIRACLS ion source in the future. The first approach would be to take full advantage of the activation process by flashing and then activating the filament for at least 30 min prior to operation. Long-term operation temperatures would need to be chosen such as not to exceed 1800 K. This mode of operation was shown to yield $5 - 6\,\mathrm{mA}$ at 6 W. Advantages of this mode of operation would be the very low operating temperatures minimising the effect of the filament heating on the oven as well as the possibility to operate on the brink of the space-charge-limited regime. Long-term testing of this mode of operation would be required to ensure its lasting stability. A second mode of operation would not take advantage of the thorium within the filament and aim at operation far within the space-charge-limited regime. One obvious drawback of this approach is the increase in the required heating power, which is even more significant due to slow rise in electron currents with temperature in the space-charge-limited regime as well as the T^4 dependency of the heating power shown in appendix A. Advantages are higher total grid currents from 6 mA at 20 W up to 8.4 mA at 30 W. However, these currents would also be expected to be easily achievable within the first mode of operation by doubling the number of short filaments on each side and heating each filament with $5 - 6\,\mathrm{W}$.
The next step foreseen in the optimisation of the ion source is a study of the dependency of the Mg^+ ion current on the electron current and an optimisation of the

Mg^+ ion yield. For the study one must carefully chose the means by which the electron current, is varied, as varying $\Delta U = U_{grid} - U_{filament}$ does not only change the number, but also the energy of the electrons and U_{mesh} has a yet to be determined focusing or defocusing effect, which both potentially change the ion yield.
In the course of the work for this thesis, a great variety of ion source parameters especially with respect to the filament have been changed, calling for a re-assessment of the horizontal position of the filament within the set-up. In addition, the configurations of electric fields was significantly changed such that a re-assessment of the optimal value of the accelerating voltage ΔU might further optimise the ion source performance.
Following careful optimisation of these parameters and an increase in the number of filament, in the first mode of operation described above, electron currents exceeding 10 mA should be readily achieved at heating powers of about 20 W making the Mg^+ ion source ready for standard operation within MIRACLS.

A. Calculation of the Filament Temperature

This appendix discusses the method for extracting the temperature of the cathode filament employed throughout this thesis. The easiest and most straight-forward way of estimating the temperature of a tungsten wire is to exploit the increase in resistivity that comes with an increase in temperature [23]. As the thorium content in the wire is in the order of 1%, the effect on its presence on the filament resistivity is neglected. The resistivity of the wire is obtained from the filament dimensions and the voltage U_H and current I_H at the filament heating power supply. The obtained values are then compared to values tabulated against temperature in the literature. In the first step, Ohm's law is employed in order to obtain the resistance of the wire

$$R = \frac{U_H}{I_H}. \tag{A.1}$$

From this value the resistivity ρ was then calculated

$$\rho = R\frac{A}{l}, \tag{A.2}$$

where A corresponds to the cross sectional surface πr^2 of the filament. In order to identify the function T of ρ best suited for use in this thesis, different results from literature were compared with one another. Fits to data obtained in [18] and [31] were found to match the temperature range of relevance for the tests conducted in this thesis and are in good agreement with one another. Therefore the temperature was calculated using the equation given in [18]

$$T = -0.0498\rho^2 + 35.84\rho + 129.1, \tag{A.3}$$

which is based on a second order fit to data. The temperature T is plotted as a function of ρ in Figure A.1. The most important systematic uncertainties are

introduced by changes in resistance due to contaminants within the wire and the cooling effects of the leads [23]. The resistance of the leads to the filaments in the MIRACLS ion source set-up were measured and found to be negligible compared to the wire resistance especially in the high temperature regime of $T > 1000\,\mathrm{K}$ relevant for measurements in this thesis. In order to study how the required heating

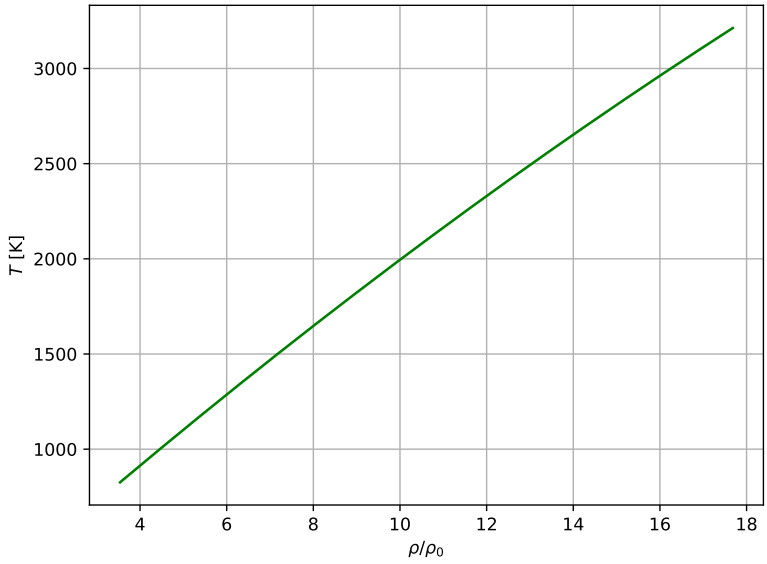

Figure A.1.: Filament temperature T as a function of resistivity ρ. Created based on [18].

power P increases with T, the two parameters were plotted in Figure A.2 for two different states of filament activation. The heating power required to reach a given filament temperature is in good agreement for the two cases. Small differences can likely be attributed to the heating of the filament prior to these measurements. The power required to achieve a given temperature increases very fast with temperature. A power fit yields a power of approximately 4, in reasonable agreement with the expectation from the Stephan-Boltzmann law.

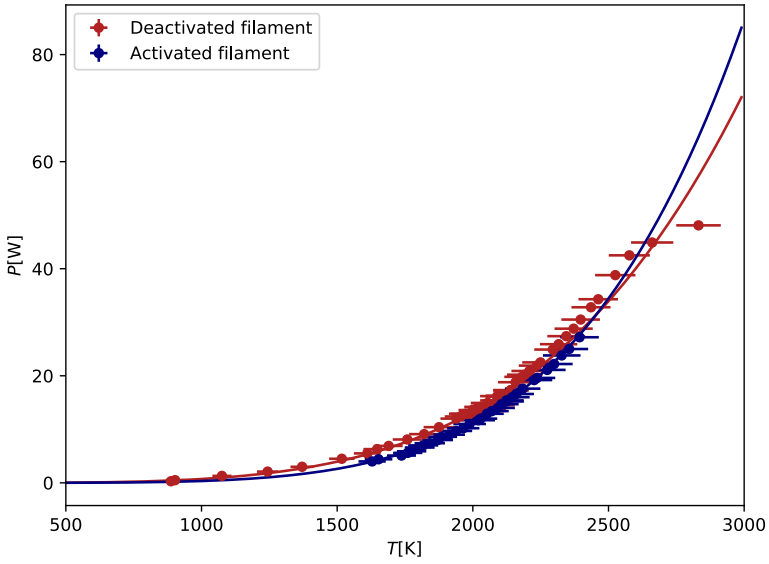

Figure A.2.: Filament heating power P as a function of temperature T. The datasets correspond to those shown in Figure 6.2(b) and a power fit is plotted for both. The data was recorded for two filaments of 4 cm length each.

Bibliography

[1] A. J. Ahearn. The effect of temperature, degree of thoriation and breakdown on field currents from tungsten and thoriated tungsten. *Phys. Rev.*, 50:238, 1936.

[2] Arthur J. Ahearn and Joseph A. Becker. Electron microscope studies of thoriated tungsten. *Phys. Rev.*, 54:448, 1938.

[3] J. D. Alexander et al. Short pulse laser-induced dissociation of vibrationally cold, trapped molecular ions. *J. Phys. B*, 42:154027, 2009.

[4] Paul J. Angiolillo. On thermionic emission and the use of vacuum tubes in the advanced physics laboratory. *American Journal of Physics*, 77:1102, 2009.

[5] W. H. Benner. A gated electrostatic ion trap to repetitiously measure the charge and m/z of large electrospray ions. *Anal. Chem.*, 69:1462, 1997.

[6] K. Blaum, J. Dilling, and W. Nörtershäuser. Precision atomic physics techniques for nuclear physics with radioactive beams. *Phys. Scr.*, T152, 2013.

[7] A. Böröczki et al. Electron stimulated thorium adatom enrichment on the surface of thoriated tungsten below 2300 K. *International Journal of Refractory Metals & Hard Materials*, 24:343–349, 2005.

[8] B. Cheal and K. T. Flanagan. Progress in laser spectroscopy at radioactive ion beam facilities. *J. Phys. G: Nucl. Part. Phys.*, 37, 2010.

[9] Wolfgang Demtröder. *Experimentalphysik 4: Kern-, Teilchen- und Astrophysik*, volume 4th edition. Springer-Verlag, 2014.

[10] F. B. Dunning and Randall G. Hulet. *Atomic, Molecular and Optical Physics: Charged Particles*. Elsevier Science & Technology, 1995.

[11] D. Edwards. Uncarburized thoriated tungsten filament activation. *Journal of Vacuum Science and Technology*, 15:128, 1978.

[12] Laurin Fischer. Improvements of the beam intensity of stable mg ions for the proof-of-principle experiment of collinear laser spectroscopy on short-lived nuclides in a multi ion reflection apparatus. B.Sc. Thesis, Karlsruhe Institute of Technology, 2017.

[13] P. E. Gear. The choice of cathode material in a hot cathode ionization gauge. *The Theory and Practice of Vacuum Science and Technology in Schools and Colleges*, 1975.

[14] H. Haken and H. C. Wolf. *Atom- und Quantenphysik. Einführung in die experimentellen und theoretischen Grundlagen*, volume 8. Auflage. Springer-Verlag Berlin Heidelberg, 2004.

[15] W. E. Harbaugh. Tunsten, thoriated-tungsten, and thoria emitters. In The editor, editor, *Electron Tube Design*, pages 90–98. Radio Cooperation of America, 1962.

[16] Harald Ibach and Hans Lüth. *Solid-State Physics: An Introduction to Principles of Materials Science*, volume Fourth Edition. Springer-Verlag Berlin Heidelberg, 2009.

[17] ISOLDE. Isolde webpage - facility. `http://isolde.web.cern.ch/facility`. Accessed: 2018-07-25.

[18] Kumar P. K. Jeethendra and Padma Jeeth Ajeya. Resistivity variation and temperature of a tungsten filament. KamalJeeth Instrumentation & Service Unit, No 610, Tata Nagar Benaguluru-560 092. INDIA.

[19] Kevin L. Jensen. *Introduction to the Physics of Electron Emission*. John Wiley & Sons Inc., 2018.

[20] Hanno Krieger. *Strahlungsquellen für Technik und Medizin*, volume 3. Auflage. Springer Spektrum, 2018.

[21] M. Lange et al. A cryogenic electrostatic trap for long-time storage of kev ion beams. *Rev. Sci. Instrum.*, 81:055105, 2010.

[22] Irving Langmuir. The effect of space charge and residual gases on thermionic currents in high vacuum. *Phys. Rev.*, 2:450, 1913.

[23] Irving Langmuir. The characteristics of tungsten filaments as functions of temperatures. *Phys. Rev.*, 7:302–330, 1916.

[24] Irving Langmuir. The effect of space charge and initial velocities on the potential distribution and thermionic current between parallel plane electrodes. *Phys. Rev.*, 21:419, 1923.

[25] Irving Langmuir. The electron emission from thoriated tungsten filaments. *Phys. Rev.*, 22:357–398, 1923.

[26] S. Malbrunot-Ettenauer et al. Benchmarking of a multi ion reflection apparatus for collinear laser spectroscopy of radionuclides. In *Letter of Intent to the ISOLDE and Neutron Time-of-Flight Committee*, 2017.

[27] Michael S. McDonald, Raymond Liang, and Alec D. Gallimore. Practical application of wide bandwidth floating emissive probes and wavelet analysis to the x2 nested hall thruster. In 33^{rd} *International Electric Propulsion Conference*, 2013.

[28] A. Modinos. *Field, Thermionic, and Secondary Electron Emission Spectroscopy.* Springer Science+Business Media New York, 1984.

[29] T. Murböck et al. A compact source for bunches of singly charged atomic ions. *Review of Scientific Instruments*, 87, 2016.

[30] R. Neugart et al. Collinear laser spectroscopy at isolde: new methods and highlights. *J. Phys. G: Nucl. Part. Phys.*, 44, 2017.

[31] Eligiusz Pawlowski. Tungsten resistance as a function of temperature. `http://elektron.pol.lublin.pl/elekp/instrukcje_LV/Tungsten_resistance.pdf`. Accessed: 2018-07-19.

[32] A. T. Perez Fontenla. Scanning electron microscopy (sem) on thoriated tungsten filaments. Report Draft, 2018.

[33] A. Piechaczek et al. Development of a high resolution isobar separator for study of exotic decays. *Nucl. Instr. Meth. B*, 266:4510, 2008.

[34] W. R. Plass et al. Isobar separation by time-of-flight mass spectrometry for low-energy radioactive ion beam facilities. *Nucl. Instrum. Meth. B*, 266:4560, 2008.

[35] Jame E. Polk. Operation of thoriated tungsten cathodes. *AIP Conference Proceedings*, 271:1435, 1993.

[36] P. A. Redhead. The birth of electronics: Thermionic emission and vacuum. *Journal of Vacuum Science & Technology A*, 16:1394–1401, 1998.

[37] RILIS. Rilis elements database - magnesium. `http://riliselements.web.cern.ch/riliselements/index.php?element=Mg`. Accessed: 2018-04-23.

[38] Petr Schneider. Thermionic emission of thoriated tungsten. *The Journal of Chemical Physics*, 28:675, 1958.

[39] P. Schury et al. Multi-reflection time-of-flight mass spectrograph for short-lived radioactive ions. *Eur. Phys. J. A*, 42:343–349, 2009.

[40] Simion. Simion webpage - child's law. `http://simion.com/`, . Accessed: 2018-07-22.

[41] Simion. Simion webpage - child's law. `http://simion.com/definition/childs_law.html`, . Accessed: 2018-07-19.

[42] Felix Stabel. Characterisation of a mg offline ion source for miracls - a multi ion reflection apparatus for collinear laser spectroscopy of short-lived radionuclides. B.Sc. Thesis, Karlsruhe Institute of Technology, 2017.

[43] F. Wienholtz et al. Masses of exotic calcium isotopes pin down nuclear forces. *Nature*, 498:346–349, 2013.

[44] Bernhard Wolf, editor. *Handbook of Ion Sources*. CRC Pres, 1995.

[45] R. N. Wolf et al. Isoltrap's multi-reflection time-of-flight mass separator/spectrometer. *Int. J. Mass Spectrom.*, 349-350:123–133, 2013.

[46] H. Wollnik and M. Przewloka. Time-of-flight mass spectrometers with multiply reflected ion trajectories. *Int. J. Mass Spectrom.*, 96:267, 1990.

[47] D. Zajfman et al. Electrostatic bottle for long-time storage of fast ion beams. *Phys. Rev. A*, 55:1577, 1997.

[48] Huashun Zhang. *Ion Sources*, volume Fourth Edition. Springer Press, 1999.

Acknowledgements

First of all I would like to thank Stephan Malbrunot for the opportunity to come to CERN, and more specifically ISOLDE, for my Bachelor's thesis on the MIRACLS project. The ISOLDE community has been very welcoming and working on my B.Sc. project in such a diverse and international research facility has been an enriching experience. A thank you is also well deserved for my colleagues working on the MIRACLS project, who offered a helping hand whenever I needed one.
My gratitude also goes to Professor Hofsäss for agreeing to act as the second referee for this thesis and without whom this thesis would not have been possible.
I would like to take the opportunity to say thank you once again to the Materials and Metrology department and especially Anite, who contributed to this thesis in the form of SEM and EDX analysis with great enthusiasm and patiently answered all of my questions regarding the investigation.

Erklärung Ich versichere hiermit, dass ich die vorliegende Arbeit ohne fremde Hilfe selbstständig verfasst und nur die von mir angegebenen Quellen und Hilfsmittel verwendet habe. Wörtlich oder sinngemäß aus anderen Werken entnommene Stellen habe ich unter Angabe der Quellen kenntlich gemacht. Die Richtlinien zur Sicherung der guten wissenschaftlichen Praxis an der Universität Göttingen wurden von mir beachtet. Eine gegebenenfalls eingereichte digitale Version stimmt mit der schriftlichen Fassung überein. Mir ist bewusst, dass bei Verstoß gegen diese Grundsätze die Prüfung mit nicht bestanden bewertet wird.

Göttingen, den July 26, 2018

(Lara Maria Bartels)